COMPARATIVE STUDIES OF CARBORANETHIOL SELF-ASSEMBLED MONOLAYERS ON GOLD SURFACES

A THESIS SUBMITTED TO
THE GRADUATE SCHOOL OF NATURAL AND APPLIED SCIENCES
OF
MIDDLE EAST TECHNICAL UNIVERSITY

BY

CANER YALÇIN

IN PARTIAL FULFILLMENT OF THE REQUIREMENTS
FOR
THE DEGREE OF MASTER OF SCIENCE
IN
MICRO AND NANOTECHNOLOGY

JANUARY 2025

Approval of the thesis:

COMPARATIVE STUDIES OF CARBORANETHIOL SELF-ASSEMBLED MONOLAYERS ON GOLD SURFACES

submitted by **CANER YALÇIN** in partial fulfillment of the requirements for the degree of **Master of Science** i**n Micro and Nanotechnology, Middle East Technical University** by,

Prof. Dr. Naci Emre Altun
Dean, **Graduate School of Natural and Applied Sciences** _____

Prof. Dr. Deniz Üner
Head of the Department, **Micro and Nanotechnology** _____

Assoc. Prof. Dr. Mehmet Fatih Danışman
Supervisor, **Micro and Nanotechnology, METU** _____

Assoc. Prof. Dr. Selçuk Yerci
Co-Supervisor, **Micro and Nanotechnology, METU** _____

Examining Committee Members:

Prof. Dr. Gülay Ertaş
Chemistry, METU _____

Assoc. Prof. Dr. Mehmet Fatih Danışman
Chemistry, METU _____

Prof. Dr. İrem Erel Göktepe
Chemistry, METU _____

Prof. Dr. Okan Esentürk
Chemistry, METU _____

Assist. Prof. Dr. Erol Albayrak
Metallurgical and Materials Eng., Kırşehir Ahi Evran Uni. _____

Date: 07.01.2025

I hereby declare that all information in this document has been obtained and presented in accordance with academic rules and ethical conduct. I also declare that, as required by these rules and conduct, I have fully cited and referenced all material and results that are not original to this work.

Name Last name : Caner Yalçın

Signature :

ABSTRACT

COMPARATIVE STUDIES OF CARBORANETHIOL SELF-ASSEMBLED MONOLAYERS ON GOLD SURFACES

Yalçın, Caner
Master of Science, Micro and Nanotechnology
Supervisor : Assoc. Prof. Dr. Mehmet Fatih Danışman
Co-Supervisor: Assoc. Prof. Dr. Selçuk Yerci

January 2025, 90 pages

The behavior, structure, and stability of carboranethiol self-assembled monolayers on gold and, occasionally, silver substrates were investigated. Primary attention was given to how molecular structure and bonding preferences will influence the properties of these SAMs. Morphology, thickness, and chemical composition assessment were conducted through the application of a systematic analysis via contact angle measurements, spectroscopic ellipsometry, atomic force microscopy, and X-ray photoelectron spectroscopy. The experimental results show that the SAMs prepared under base-free and basic conditions do not differ much in morphology or surface characteristics, hence removing the necessity to prepare basic solutions. Comparison studies on bis-carboranethiol isomers illustrate that the para-substituted isomer, pp-SH, self-assembles into more ordered, stable, and defect-free monolayers compared to its meta-substituted isomer, mm-SH. Thickness measurements support the smoothness and homogeneity of the pp-SH surface, making this a promising precursor for applications where stable and uniform monolayers are required. Another point that was underlined is the thermodynamic preference of the bonding interactions, which means that on gold surfaces, P1C SAMs with Au-S-C bonds are much more stable than diMe-O9 SAMs containing Au-S-B bonds. The replacement

experiments indeed showed that, over time, the P1C SAMs will dominate because of their favorable thermodynamic properties. On silver substrates, however, weaker binding interactions and high surface roughness lead to reduced stability and selectivity, resulting in less organized monolayers and significant intermixing.

Keywords: Carboranethiol, Self-Assembled Monolayer, Contact Angle

ÖZ

KARBORANTİYOL KENDİLİĞİNDEN DÜZENLENEN TEK KATMANLI YAPILARIN (KDT) ALTIN YÜZEY ÜZERİNDEKİ DAVRANIŞLARININ KIYASLAMALI BİR ŞEKİLDE İNCELENMESİ

Yalçın, Caner
Yüksek Lisans, Mikro ve Nanoteknoloji
Tez Yöneticisi: Doç. Dr. Mehmet Fatih Danışman
Ortak Tez Yöneticisi: Doç. Dr. Selçuk Yerci

Ocak 2025, 90 sayfa

Karborantiyol kendiliğinden düzenlenmiş tek-tabaka (KDT) filmlerin altın ve bazen de gümüş alttaşlar üzerindeki davranışı, yapısı ve kararlılığı araştırılmıştır. Bu tür koşullarda, moleküler yapı ve bağlanma tercihlerinin bu KDT'lerin özellikleri üzerindeki deneysel koşulların değişimini nasıl etkileyeceğine öncelik verilmiştir. Morfoloji, kalınlık ve kimyasal bileşim değerlendirmesi, temas açısı ölçümleri, spektroskopik elipsometri, atomik kuvvet mikroskobu ve X-ışını fotoelektron spektroskopisi yoluyla sistematik bir analiz uygulanarak gerçekleştirilmiştir. Deneysel sonuçlar, bazik ve bazik olmayan koşullar altında hazırlanan KDT'lerin morfoloji veya yüzey özellikleri açısından çok farklı olmadığını, dolayısıyla bazik koşullara gerek olmadığını göstermiştir. Bis-karborantiyol izomerleri üzerinde yapılan karşılaştırma çalışmaları, para-sübstitüe izomer pp-SH'nin, meta-sübstitüe izomeri mm-SH'ye kıyasla daha düzenli, kararlı ve hatasız tek katmanlar halinde kendiliğinden birleştiğini göstermektedir. Kalınlık ölçümleri pp-SH yüzeyinin pürüzsüzlüğünü ve homojenliğini desteklemekte, bu da onu kararlı ve düzgün bir tek tabakanın gerekli olduğu uygulamalar için umut verici bir öncü haline getirmektedir. Altı çizilen bir diğer nokta da bağ etkileşimlerinin termodinamik tercihidir; bu da

altın yüzeylerde Au-S-C bağlarına sahip P1C KDT'lerin Au-S-B bağları içeren diME-O9 SAM'lerden çok daha kararlı olduğu anlamına gelmektedir. Yer değiştirme deneyleri gerçekten de zaman içinde P1C KDT'lerin elverişli termodinamik özellikleri nedeniyle baskın olacağını göstermiştir. Bununla birlikte, gümüş alt tabakalarda, daha zayıf bağlanma etkileşimleri ve yüksek yüzey pürüzlülüğü ile, kararlılığın ve seçiciliğin azalmasına yol açar, bu da sonuçta daha az organize tek katmanlara ve moleküler düzeyde karışmaya neden olur.

Anahtar Kelimeler: Karborantiyol, Kendiliğinden Düzenlenmiş Tek-Tabaka,
Temas Açısı

To my family

ACKNOWLEDGMENTS

I would like to express my deepest gratitude to my supervisor Assoc. Prof. Dr. Mehmet Fatih Danışman and co-supervisor Assoc. Prof. Dr. Selçuk Yerci for their guidance, advice, criticism, encouragement, and insight throughout the research. I would like to thank all jury members for their time and patience.

Special thanks to Adem Yavuz for helping me during this study and sharing his experience.

I would also like to thank Dr. Tomáš Baše for providing carboranethiol isomers, and for his hospitality.

I express my sincere thanks to my friends who showed valuable support; Batuhan Uzun, Firdevs Aydın, Ersoy Aymak, Kaan Arslan, Derya Hazal Yıldırım.

I am grateful to my parents and brother for their support and confidence in me.

This work is partially funded by Scientific and Technological Research Council of Turkey under grant number TUBİTAK 120N628.

TABLE OF CONTENTS

LIST OF TABLES

TABLES

LIST OF FIGURES

FIGURES

LIST OF ABBREVIATIONS

ABBREVIATIONS

SAM	Self-Assembled Monolayer
DSA	Directed Self-Assembly
STM	Scanning Tunneling Microscopy
TSAu	Template-Stripped Gold
SHG	Second Harmonic Generation
CVD	Chemical Vapor Deposition
SMBD	Supersonic Molecular Beam Deposition
OBS	Organic Beam Source
SH	Sample Holder
DFT	Density Functional Theory
FTIR	Fourier-Transform Infrared Spectroscopy
XPS	X-ray Photoelectron Spectroscopy
AFM	Atomic Force Microscope
CA	Contact Angle
NMR	Nuclear Magnetic Resonance
GC/MS	Gas Chromatography-Mass Spectrometry
QCM	Quartz Crystal Microbalance
O1	o-Carborane-1-Thiol
O9	o-Carborane-9-Thiol

P1C	Carboxylated p-Carborane-1-Thiol
diMe-O9	Dimethylated o-Carborane-9-Thiol
mm-SH	1,1’-bis-m-Carborane-7-Thiol
pp-SH	1,1’-bis-p-Carborane-12-Thiol
M1	m-Carborane-1-Thiol
M9	m-Carborane-9-Thiol
ODT	1-Octadecanethiol
DT	1-Decanethiol
DI	Deionized
GC	Glycerol
EG	Ethylene Glycol
DMSO	Dimethyl Sulfoxide

CHAPTER 1

INTRODUCTION

1.1 Background

The study of organic thin films has gained attention in the last few decades as a result of technological advancements, but it roots back to the 18th century with the studies of oil-water interfaces [1]. I. Langmuir achieved a significant milestone by publishing his studies of molecular thin films at liquid-gas interfaces [2], [3], which investigates the behavior of fatty acids on the water surface. Different groups of molecules are emphasized while explaining the formation of the thin film. Hydrophilic parts of these molecules show affinity to water; they are soluble in water, but the hydrophobic parts of molecules orient themselves opposite to water. This occurrence results in perfectly ordered monolayers on the water surface. Building upon this praxis, Blodgett was the first to introduce the deposition of long-chain carboxylic acids on solid substrates [4], [5]. The process involves slowly raising the solid substrate from the water where the Langmuir film was prepared. The film attaches itself to the substrate with receding water on the surface. The formation of ordered thin films on a surface is called the process of self-assembly. Zisman, Blackman, and Dewar further studied the topic [1], which constitutes the foundations of self-assembled monolayers (SAMs). Unlike their times, much more advanced characterization techniques are available today, which allow us to form advanced correlations between the microscopic and macroscopic properties of SAMs.

There are different routes to prepare SAMs from liquid and gas phases, but the most readily available method is growing SAMs from a solution. In Figure 1.1,

representative drawings of the process can be seen along with Langmuir and Langmuir-Blodgett films. To summarize, the power of self-assembly process allows molecules to order on a solid surface without external intervention. SAMs grown in the gas phase will also be discussed in further parts of the thesis.

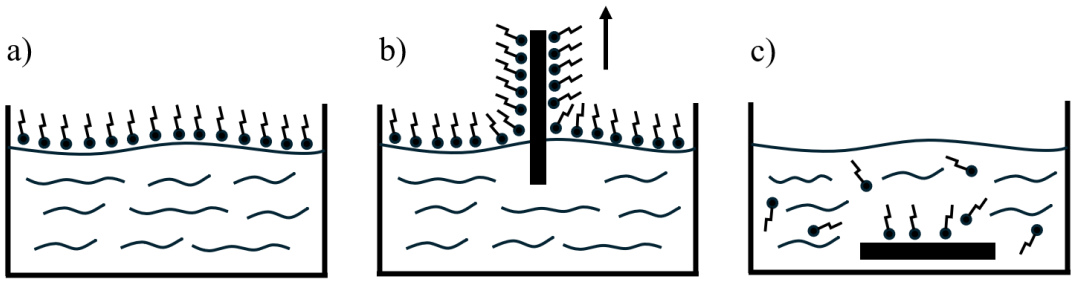

Figure 1.1. Schematic depictions of a) Langmuir films, b) Langmuir-Blodgett films, and c) self-assembled monolayers grown from solution.

1.2 The self-assembly process

Self-assembly is the process where simpler building blocks spontaneously form hierarchically complex structures without human intervention [6], [7]. These building blocks, or adsorbents, have to show some kind of affinity to the surface to build up crystalline or semicrystalline structures. Interactions between the adsorbents also play crucial roles although they are governed by weak, noncovalent bonds. These weak interactions like hydrogen bonds, van der Waals forces, and electrostatic interactions build up to direct spatial conformity of the ordered, secondary structure [8]. The most common example of the self-assembly process is the one that takes place in SAMs. However, viruses, cellular structures, and biological membranes can all be regarded as complex self-assembly systems. There are many examples in biological systems where nanostructures form a complex network [7], but those are not in the scope of this thesis.

In SAMs, adsorbent structures have different groups, or parts, which can be divided into three: the headgroup (or ligand), molecular backbone, and terminal functional (active) group [9]. The headgroup mainly dominates the self-assembly process by

guiding the adsorbent to the substrate, accountable for chemical (covalent) bonding. Different types of headgroups will go well with different substrates. The most important ones for the context of this thesis are thiols (RHS). They constitute strong bonds with Au, Ag, Cu[10], Pt[11], Ge[12], Hg[13], Ni[14], Ir[15], Zn[16], GaAs[17], etc. substrates. The strong interactions between the headgroup and the substrate are the foremost mechanism of self-assembly. The backbone group is responsible for noncovalent weak interactions, creating a driving force that drives the system to a new thermodynamic minimum [18], [19]. Properties like molecular dimensions play a vital role in defining supramolecular structures. The terminal functional group is responsible for surface properties like wettability. It can also act as an anchor for bindings of different molecules, which are the main governors of the dipole moment- in SAMs with long alkyl chains [20]. Thus, it might have a great influence on supramolecular structure.

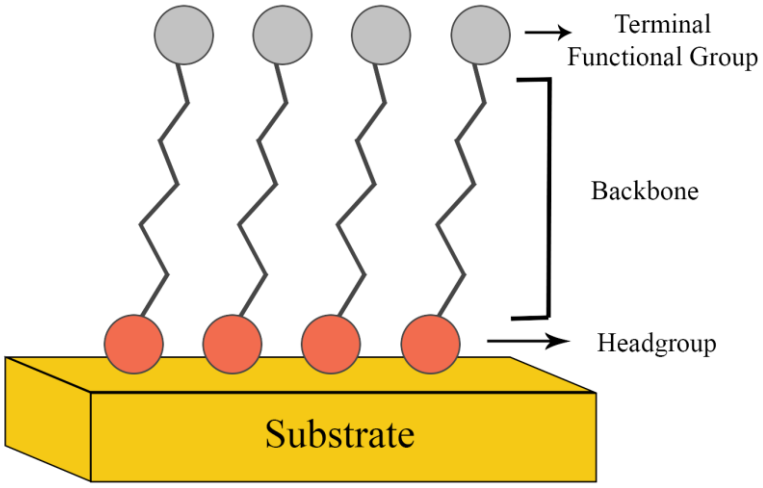

Figure 1.2. Schematic of different groups in a self-assembled structure.

One of the important matters that should be mentioned is directed self-assembly (DSA). It is an emerging technique still under development, which enhances current patterning methods by integrating them with self-assembly processes [21]. By modulating the driving thermodynamic forces of self-assembly, the process can be controlled and directed. These can be done by either templating or rational use of chemistry [22]. Templates can be considered as frameworks that complement the

morphology of the desired assembly. They can be categorized into soft and hard templates. Hard templates comprise rigid structures such as carbon nanotubes, whereas some flexible materials like polymers, and biomolecules can be utilized as soft templates. Instead of relying on a pre-structured template, intrinsic properties of the building blocks and surface chemistry can also be used for DSA.

1.3 Selection of substrates for thiol-based SAMs

Although SAMs of thiol compounds can be deposited on different substrates, the focus is on the Au(111) surfaces. Gold is known to be one of the most inert substances, although their nanoparticles (especially ones below 5 nm size) exhibit catalytic properties [23]. Gold crystals exhibit a face-centered cubic structure. In the (111) crystallographic direction, they arrange into a hexagonal lattice. Au(111) surface is the lowest energy configuration which exhibits higher atomic packing density [24]. For the SAM applications, smooth surfaces are required. Surfaces produced by thermal evaporation or sputtering are often rather rough. Special techniques are employed to smoothen gold surfaces like flame annealing or template stripping [25]. In addition, bulk single-crystal Au(111) substrates are critical for studies involving vacuum-deposited SAMs, where ultra-high purity and atomic-level flatness are prerequisites. These surfaces are typically prepared from bulk gold single crystals, which are mechanically and electrochemically polished to expose the (111) facet, followed by repeated cycles of argon-ion sputtering and annealing in ultra-high vacuum (UHV) to remove contaminants and defects.

The flame annealing process aims to improve the atomic order of the substrate and get rid of the surface contaminants. This is done by heating the substrate to produce single-crystalline larger grains, effectively reducing the number of boundaries and increasing grain size. Maver et al. detail a new annealing technique [26], involving the annealing of gold-coated mica substrates in a hydrogen flame setup. Annealing of the mica-gold substrates is in such a way that the temperature can be precisely controlled to obtain a homogenous flat surface on the substrate. In the optimized

technique, flat terraces would result in the substrate absent of any grain structures, the common flaws in previous techniques.

Template-stripping is a more controlled technique for achieving ultra-smooth surfaces, which does not pose any danger of handling a hydrogen torch. The method involves the deposition of gold onto a template, chosen to be flat. Usual templates are polished silicon or mica, which has atomic-level smoothness. A solid support is then attached with a proper adhesion layer and gold is cleaved from the template. The smoothness of the template is often projected onto the gold surface with this method. The process will be detailed in Chapter 2, due to it being the main method for the substrate preparation for the context of this thesis. In Figure 1.3, scanning tunneling microscope (STM) images of template-stripped gold (TSAu) surface and a monolayer grown on top of it are shown. The hexagonal lattice structure of (111) surface can be seen with minimal defects. The template-stripping process also comes with its drawbacks, mainly due to difficulties with the mechanical cleaving of the substrate. The adhesion layer, which usually contains organic compounds, might also interfere with some applications such as vacuum deposition of SAMs. Specifically, organic adhesion layers can outgas under low-pressure conditions, compromising vacuum integrity. In contrast, bulk single-crystal Au(111) substrates, which lack adhesives, are preferred for SAM deposition in high-vacuum environments like molecular beam deposition chambers. However, the template-stripping method is generally clean and easy to implement.

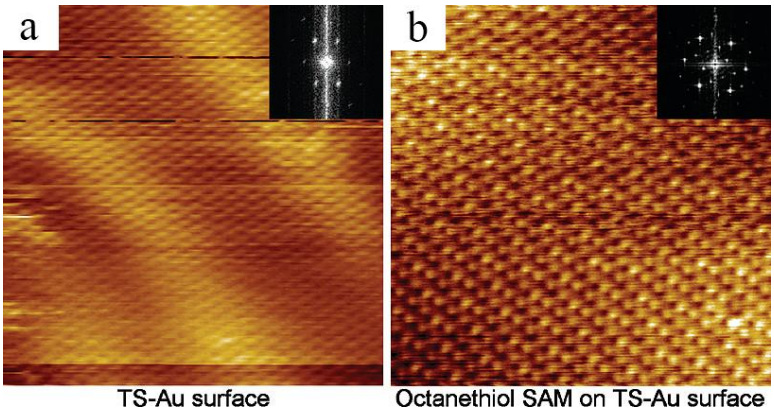

Figure 1.3. STM images of (a) 10 nm × 10 nm TSAu surface (b) 15 nm × 15 nm TSAu surface dosed with octanethiol, retrieved from ref [27].

1.4 Methods of SAM growth

In this section, SAM deposition methods, mainly liquid-solid, and vapor-solid interfaces, will be discussed. The SAM growth process typically focuses on immersing the substrate into a proper solution, and allowing molecules to self-assemble; however vapor-phase deposition has its advantages. A detailed review is needed comparing these two methods.

1.4.1 Liquid-phase deposition

The liquid-phase method offers the benefit of allowing the solution to easily interact with the reaction surface during the self-assembly process, which makes the process straightforward. However, the exact kinematics of the growth process are less controllable, leading to difficulties in achieving reproducible surfaces [28]. The cleanliness of the solution is a parameter to consider, as well as control of the exact concentration. If the substrates are contaminated before immersion, the growth of SAMs could be delayed, although most of the contamination is eventually replaced [29]. The adsorption kinetics can generally be described using three classical variations of the Langmuir kinetic models [30].

$$\theta(t) = 1 - e^{-k_{FO}ct} \quad (1)$$

This equation represents the first-order Langmuir kinetics, taking only chemisorption into account. Here, θ represents the coverage, k denotes the rate constant, t is time, and c is the molecular concentration of the solution.

$$\theta(t) = \frac{1}{1 - (1 + k_{SO}ct)} \quad (2)$$

Equation 2 accounts for physisorption prior to chemisorption and follows second-order kinetics.

$$\theta(t) = 1 - e^{-k_{DL}c\sqrt{t}} \quad (3)$$

Equation 3 represents diffusion-limited Langmuir kinetic. It is often seen at low concentrations. The limiting element for adsorption in this model is the diffusion of molecules from the solution to the substrate surface.

Experimental determination of surface coverage with high accuracy is possible with a phenomenon called second harmonic generation (SHG) [31]. SHG occurs when two photons of the same frequency (ω) interact with a nonlinear material and combine to form a new photon with twice the energy (2ω), effectively doubling the frequency. SHG intensity is measured at various stages of SAM formation, which can be correlated to surface coverage. Dannenberger et al. investigated the adsorption kinetics of n-alkanethiols onto gold substrates using SHG [32]. They found that Langmuir kinetics best fit the data they got. The time-dependent surface coverage of dodecanethiol can be seen in Figure 1.4. Adsorption process primarily goes through chemisorption without a significant physisorbed intermediate.

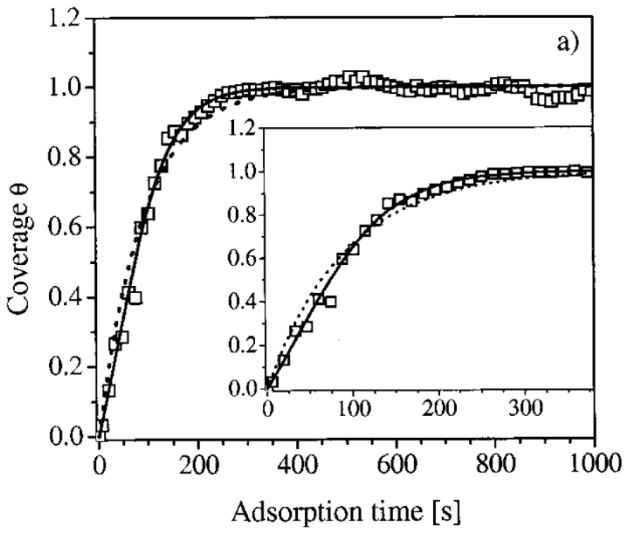

Figure 1.4. Surface coverage of dodecanethiol monolayer from hexane solution is plotted. Time-dependent coverage is determined from SHG measurements (□). Data is fitted based on Langmuir kinetics (dotted line), and a precursor model (solid line). Retrieved from ref [32].

In the monolayer formation, most of the chemisorption occurs within minutes, achieving rapid initial surface coverage. The remaining process proceeds more slowly as the system approaches a saturation level, where the molecules reorganize to form a densely packed monolayer.

1.4.2 Vapor-phase deposition

Vapor-phase deposition process involves exposing the surface to vaporized molecules with highly controlled environmental conditions, a level of control typically not achievable in liquid-phase deposition. It offers more consistent monolayer coverage over complex topographies. SAM formation in porous surfaces is especially difficult in solution deposition as molecules linked to a liquid can hardly penetrate into narrow areas, unlike in vapor-phase deposition [28]. The deposition process starts with the substrate being prepared and cleaned from all contaminants to ensure a pristine surface is available for adsorption. This step is highly crucial

because any residual impurities from the substrate will affect the SAM quality. At this point, the prepared substrate is exposed to the precursor molecules in the vapor phase. These molecules are normally deposited inside a vacuum chamber or a low-pressure reaction chamber, ensuring that the deposition parameters are very precisely controlled. Upon contact of the vapor-phase molecules with the substrate, a chemical or physical reaction of head groups with the surface results in strong bonding. Simultaneously, there is a lateral arrangement of the molecules through van der Waals interactions, hydrogen bonding, or other noncovalent forces that develop into a dense, ordered monolayer [33]. The simplest depiction of the process can be seen in Figure 1.5. The initial stage is the physisorption of molecules through weak forces, followed by the chemisorption and standing-up phase, and finally the formation of ordered monolayers. The self-assembly is thermodynamically driven as a way for the system to decrease the free energy of the molecules on the surface.

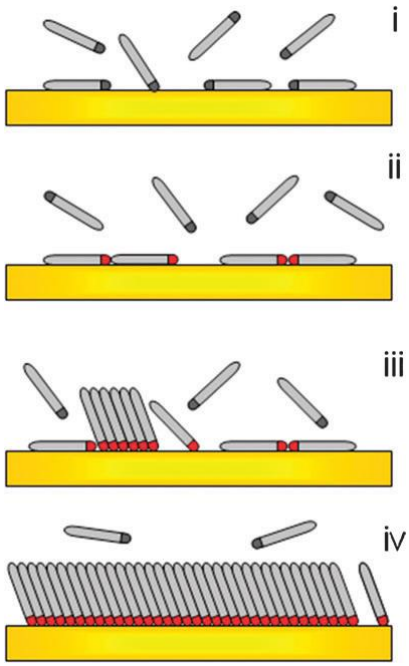

Figure 1.5. Stages of gas-phase SAM deposition of alkanethiols: (i) physisorption, (ii) lying down phase with starting of chemisorption, (iii) nucleation of standing up phase, (iv) completion of standing up phase. Retrieved from ref [9].

Most of the vapor-phase deposition techniques usually require complicated or expensive equipment such as vacuum chambers, high-temperature furnaces, or plasma chambers. This situation has caused the researchers to look for other techniques that lower the equipment requirements, like ambient-pressure vapor deposition [34]. The study by Dong and his coworkers details a chemical vapor deposition (CVD) technique for growing octadecyltrichlorosilane (OTS) monolayers onto silicon wafers and atomic force microscope (AFM) probes [35]. Conventional solution deposition methods result in aggregates of particles on the surface when dealing with small devices, such as an AFM probe. This occurs due to a potentially uncontrolled amount of water in the organic solvent, which can be minimized in the study mentioned above using the CVD method. By changing the deposition conditions, OTS-coated surfaces with static water contact angles in the range between 20° and 107° can be obtained, enabling precise control of surface hydrophobicity.

The growth phases of alkanethiols on gold surfaces are studied and reviewed in depth by Schreiber [1]. To summarize the process, initially, thiol molecules come in contact with gold surfaces in a physisorbed state, where S-H bond remains intact. These molecules eventually undergo dissociative adsorption to form chemisorbed thiolates, likely releasing hydrogen gas (H_2) in the process. Alkanethiols lie flat on the surface after the initial chemisorption and they require a significant flux of adsorbate molecules and elevated temperatures (above 200 K) to transform into upright, densely-packed SAM structures [7]. Molecules with longer chains show stronger interactions, enabling easier S-H bond dissociation. Despite its advantages, vapor-phase growth still needs flat and homogeneous surfaces to form ordered monolayers. Possible defects can be seen in Figure 1.6.

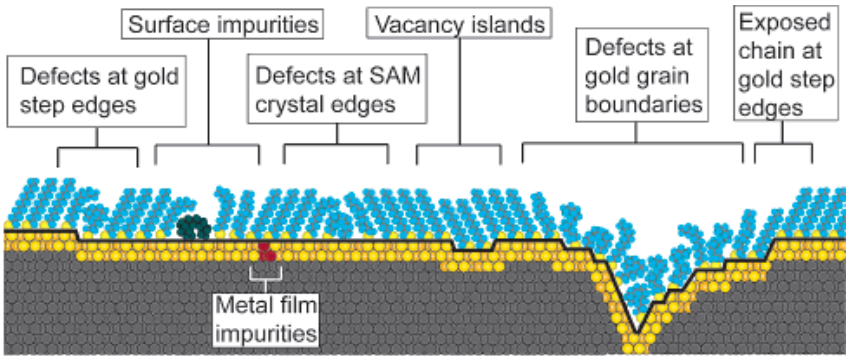

Figure 1.6. Some of the intrinsic and extrinsic defects of SAMs grown on polycrystalline substrates. Retrieved from ref [7].

In this thesis, supersonic molecular beam deposition (SMBD), a highly precise technique for growing thin films, was employed. It allows for better control over nucleation and growth mechanisms, as well as fine-tuning of the film's properties. The SMBD system contains two main vacuum chambers: the organic beam source (OBS) chamber and the sample holder (SH) chamber, separated by a shutter in front of the skimmer. The details will be explained in Chapter 2.

1.5 Thiol-based self-assembled monolayers

SAMs of thiol-based compounds are relatively easy to prepare and they can be considered powerful surface engineering tools [36]. To summarize, they can act as a physical barrier to prevent corrosion of metals [37], and they can be used to tailor surface properties like wettability and work function. SAMs of thiols also enable targeted interactions such as drug delivery and imaging in the context of biomedical applications [38]. Based on their molecular architecture, thiol-based SAMs may be categorized as: Linear alkanethiols consisting of straight-chain alkyl groups terminated by a thiol group, giving rise to simple ordered monolayers. Aromatic thiols [39] introduce aromatic rings into the molecules, providing rigidity and a conjugated π-system. Dithiol and multithiol compounds have two or more thiol groups and, hence, are able to form more stable or cross-linked monolayers. Branched and polymeric thiols introduce structural complexity that affects packing

density and the organization of the monolayer. These different architectures define the structural properties of thiol-based SAMs. Notably, alkanethiols are widely studied because of their tunable properties such as chain length. Carboranethiols, on the other hand, emerged as promising SAM building blocks that offer unique characteristics. These compounds will be reviewed in this section to better understand their roles in surface modification.

1.5.1 Alkanethiol SAMs

An alkanethiol molecule, associated with alkyl chains with different lengths, shows reactivity to metal surfaces with a thiol group. Their general formula is $HS\text{-}(CH_2)_n\text{-}X$, where 'n' denotes the number of methylene units in the chain and 'X' is a functional group that can be attached for specific applications. These molecules can be functionalized to modify their properties and are commonly used as spacer elements in molecular assemblies [40].

Highly ordered monolayers of alkanethiols can be grown on Au(111) surfaces. Sulfur atoms are anchored to the surface with the chemisorption process, whereas close packing of those molecules is ensured by van der Waals forces amongst long hydrocarbon chains. The arrangement of alkanethiols on the gold surface can be defined with $(\sqrt{3} \times \sqrt{3})$ R30° overlayer [41] or c(4 × 2) superlattice [42]. The former structure readily suggests the hexagonal symmetry with the nearest neighbor distance of 5 Å, considering it is 2.88 Å for gold atoms [9]. Area per molecule on the Au(111) surface can be calculated as 21.5 $Å^2$. The structure can also be described as c(4 × 2) superlattice, equivalent of $2\sqrt{3} \times 3$ rectangular unit cell [7], [43]. These molecular structures can be imaged using STM, as decanethiol SAM images shown in Figure 1.7.

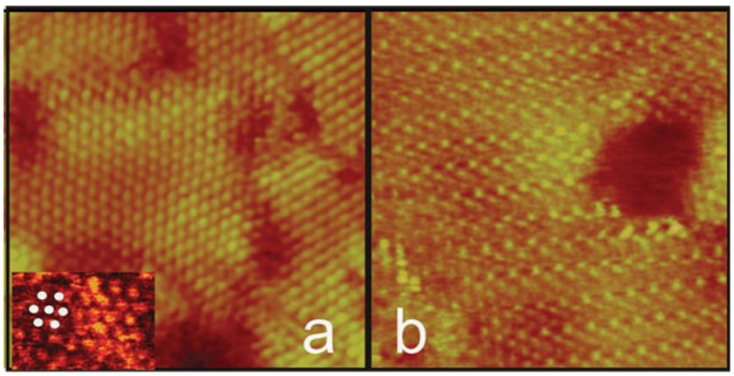

Figure 1.7. 13.5 × 13.5 nm^2 STM images of decanethiol SAMs, where bright spots are thiol molecules, (a) showing ($\sqrt{3} \times \sqrt{3}$) R30° structure, and (b) rectangular c(4 × 2) superlattice. White dots on the bottom left show a hexagonal structure. Retrieved from ref [9].

1.5.2 Carboranethiol SAMs

Carboranethiol molecules, which are the focus of this thesis, are unique molecules with their cage-like -icosahedral- structures and inherent dipole moments [44]. Their general formula can be expressed as HS-$C_2H_{11}B_{10}$, and three main variations or isomers of them are available depending on the positions of carbon atoms in the spherical structure. Atom numberings and isomers of carboranes can be seen in Figure 1.8. The ortho-carborane structure is one in which the carbon atoms are adjacent to each other. If the carbon atoms are separated by one boron atom, the structure is referred to as meta-carborane, and if they are separated by two boron atoms, it is called para-carborane. The position of the carbon atoms influences the dipole moment. Para-carboranes have no net dipole moment due to intrinsic symmetry, and ortho-carboranes have the highest dipole moment. Changing the dipole moment without changing the molecular geometry is possible.

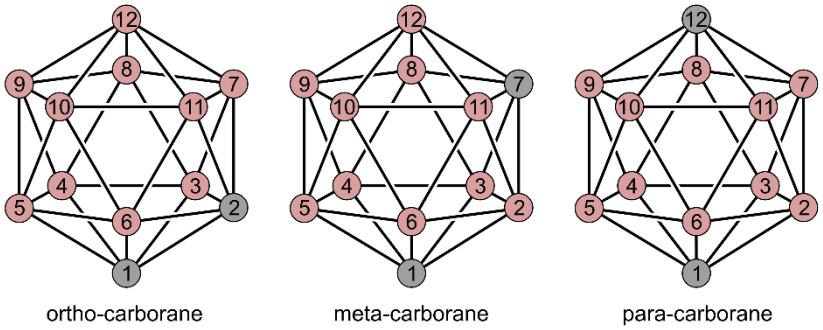

Figure 1.8. Geometrical structures of 3 different carborane isomers: ortho-carborane (1,2-$C_2B_{10}H_{12}$), meta-carborane (1,7-$C_2B_{10}H_{12}$), para-carborane (1,12-$C_2B_{10}H_{12}$). Red: boron, gray: carbon, hydrogens are omitted.

Schwartz et al. investigated how dipole characteristics of carboranethiol SAMs affect the alignment of liquid crystals [45]. They created SAMs with different dipole orientations and analyzed how these surfaces affected the in-plane orientation and anchoring energies of liquid crystals. Carboranethiols can also be configured as dithiols by attaching two thiol groups to the carborane; however, this thesis primarily focuses on single thiolated derivatives. Moreover, carborane cage significantly reduces defect formation in SAMs to result in compact and highly-ordered monolayers [46].

A remarkable feature of the icosahedral carborane structures is the hexacoordination of carbon and boron atoms. The structure is electron deficient due to boron hydrides, leading to delocalized bonding [47]. Due to this nature, their SAMs offer enhanced thermal and oxidative stability. Carboranethiols can also be functionalized with various substituents, carboxyl [48] and methyl [49] groups. Carboxyl-functionalized SAMs can enhance surface hydrophilicity and they are useful for biosensing and biomolecular attachment, while methyl-functionalized SAMs provide increased hydrophobicity, suitable for protective coatings and anti-corrosive layers. Yortanlı et al. studied how different functional groups (-NO_2, -CHO, -$CONH_2$, -F, -Cl, -OH) on carboranethiol monolayers affect their electrochemical properties on Au(111) surfaces [50]. By using density functional theory (DFT), researchers found that functional groups allow the work function of the modified gold surface to change

widely (from 5.57 to 3.49 eV). The study highlights the tunable properties of carboranethiol SAMs.

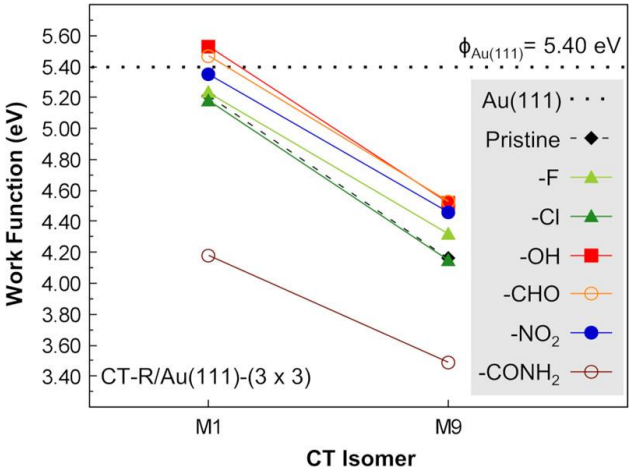

Figure 1.9. Calculated work functions of the Au(111) surface coated with M1 (1-(HS)-1,7-$C_2B_{10}H_{11}$) and M9 (9-(HS)-1,7-$C_2B_{10}H_{11}$) derivatives functionalized with -F, -Cl, -OH, -CHO, -NO_2, and -$CONH_2$ groups in a (3 × 3) surface configuration. The horizontal dotted line represents the work function of the uncoated Au(111) surface, measured at 5.40 eV. Retrieved from ref [50].

In a study by Hohman et al. investigating the carboranethiol surfaces with STM, well-ordered hexagonal lattices were observed with a lack of domain boundaries and vacancy islands [47]. They investigated monolayers of 1-(HS)-1,7-$C_2B_{10}H_{11}$ (M1) and 9-(HS)-1,7-$C_2B_{10}H_{11}$ (M9) carboranethiol derivatives. The unit cell structure was found to be (√19 × √19) R23.4° for both isomers as their geometric structures are identical. This structure gives a nearest-neighbor spacing of approximately 7.2 Å, which is in agreement with the geometry of the carborane molecules. Although no vacancy islands were observed, some rotational domains were indeed observed using STM. Grazing Incidence Fourier Transform Infrared (FTIR) Spectroscopy was used to investigate the specific bonding and surface organization of M1 and M9. In each isomer, B-H stretching peaks were observed, which can easily distinguish M1 and M9 when mixed monolayers are present.

SAMs were co-deposited from solutions containing varying ratios of M1 and M9 in the adsorption experiments. FTIR analysis showed that M1 had a higher surface coverage even when it was less concentrated in solution. This preference was attributed to favorable dipole-dipole interactions within M1 SAMs, which stabilize the monolayer.

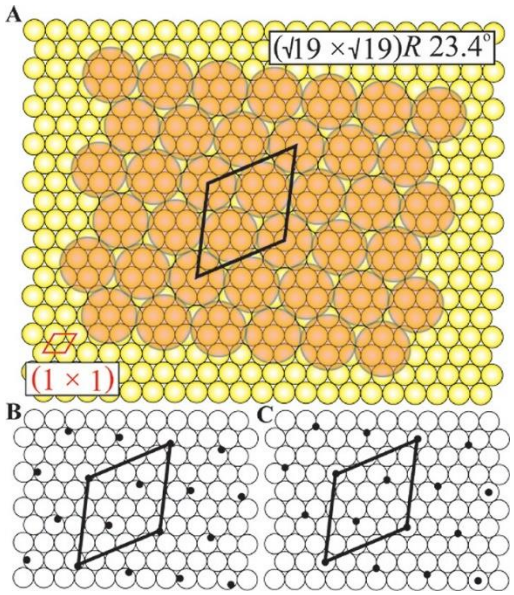

Figure 1.10. Depictions of (√19 × √19) R23.4° unit cell structures M1 and M9 isomer or their mixtures are shown here. Panels (a) and (c) illustrate alternating atop and 3-fold hollow configurations, while panel (b) shows an equivalent near-bridge configuration. Retrieved from ref [47].

As a starting point for this thesis, SAMs of 1-(HS)-1,2-$C_2B_{10}H_{11}$ (O1) and 9-(HS)-1,2-$C_2B_{10}H_{11}$ (O9) molecules were characterized. The structures of these molecules can be seen in Figure 1.11. Comparative studies were performed between these two molecules to be able to comprehend the effects of chemical differences on the SAM quality. O1 and O9 were both expected to primarily form stable monolayers with thiolate bonds to gold. O9, with its H-S-B bond, was hypothesized to differ in electron density withdrawal compared to the H-S-C bond of O1. Complementary to this, SAMs of 9-(HS)-1,2-$(CH_3)_2$-1,2-$C_2B_{10}H_9$ (diMe-O9) and 1-(HS)-12-(COOH)-1,12-$C_2B_{10}H_{10}$ (P1C) were also studied. Different functional groups of these

molecules change the hydrophobicity of the SAM surface, which makes comparative characterization via contact angle goniometry applicable.

SAMs of 1,1’-bis(1,7-$C_2B_{10}H_{10/11}$)-7-(HS) (mm-SH) and 1,1’-bis(1,12-$C_2B_{10}H_{10/11}$)-12-(HS) (pp-SH) molecules were studied in the second part of the thesis, whose can be roughly described as two carborane molecules bonded together with the addition of thiol groups. These molecules, whose has delicate synthesis processes, were expected to form more complex structures due to the need to consider longitudional dipole interactions within their SAMs. Their monolayers facilitate a transition from monolayers to more complex three-dimensional structures. This provides a platform for exploring new surface interactions. Their structure, again, can be seen in Figure 1.11. More surface coverage was expected because of the extra carborane.

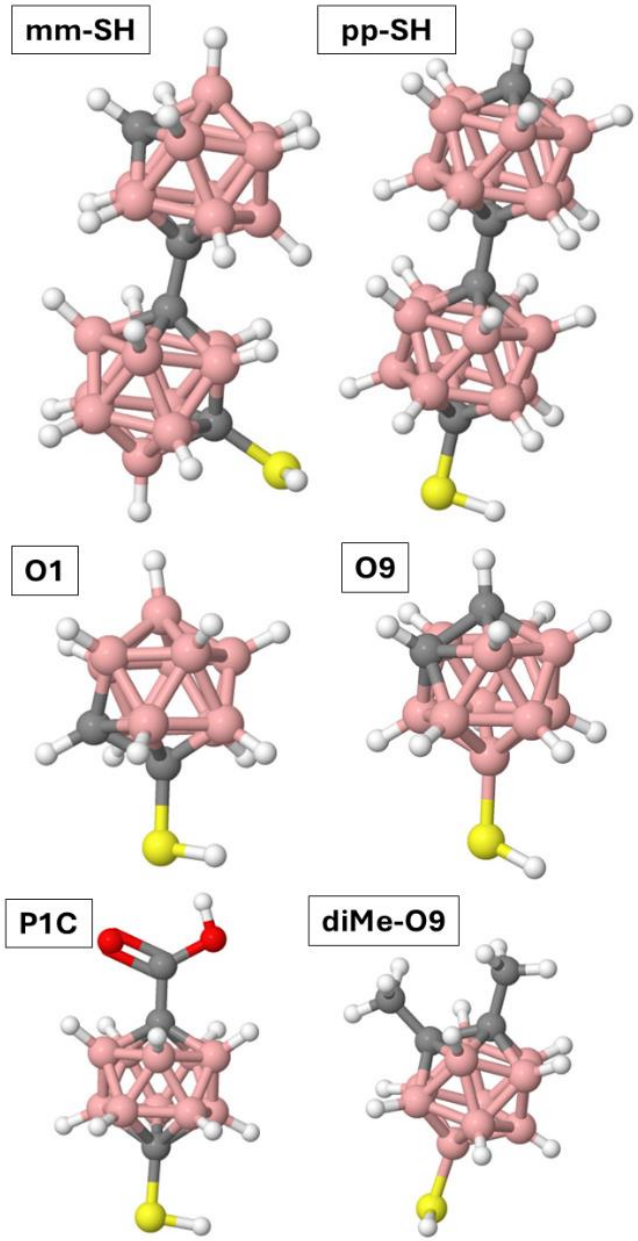

Figure 1.11. Optimized structures of thiolated molecules that were characterized in this thesis: 1,1'-bis(1,7-$C_2B_{10}H_{10/11}$)-7-(HS) (mm-SH), 1,1'-bis(1,12-$C_2B_{10}H_{10/11}$)-12-(HS) (pp-SH), 1-(HS)-1,2-$C_2B_{10}H_{11}$ (O1), 9-(HS)-1,2-$C_2B_{10}H_{11}$ (O9), 9-(HS)-1,2-$(CH_3)_2$-1,2-$C_2B_{10}H_9$ (diMe-O9), and 1-(HS)-12-(COOH)-1,12-$C_2B_{10}H_{10}$ (P1C). Atoms are color-coded as follows: pink for boron, gray for carbon, white for hydrogen, and yellow for sulfur.

1.6 Characterization Techniques of SAMs

Self-assembled monolayers have been under intensive study for their special structure, chemical, and physical properties. In order to explain and improve these monolayers, complete characterization is important. The methods to characterize SAMs involve various domains of surface science to understand structure, composition, and functionality. Spectroscopic techniques are among the most commonly used methods. X-ray photoelectron spectroscopy (XPS) is commonly used to confirm the elemental composition and the chemical state of SAMs [51]. XPS, while providing information on the binding energies of core electrons, gives information on the molecular structure and the quality of SAMs. Microscopic techniques have become indispensable for the visualization of the surface morphology of SAMs [52]. Atomic force microscopy (AFM) is widely used for determining the surface roughness of a sample and imaging nanoscale features, which supplies direct information on the homogeneity and coverage of a monolayer. Using the force mode, one can study the interaction of a probe with the SAM and, therefore, mechanical properties such as elasticity or adhesion. Other powerful tools, such as STM, have atomic-scale resolution and thus allow the packing density and ordering of the molecules in a SAM to be investigated. Commonly, ellipsometry is used for the measurement of thicknesses in SAMs. Since ellipsometry monitors the change in polarized light reflected from the surface, thickness measurements can be precisely made by it, reflecting quality and uniformity in the monolayer. Contact angle (CA) goniometry is another quite widely used but simpler technique [53]. It evaluates the wettability of the SAM-covered surface, based on the shape that a liquid droplet assumes upon being placed on the covered surface. The contact angle reflects the surface energy and indirectly reflects the uniformity and chemical functionality of the SAM. High contact angles suggest well-ordered and hydrophobic SAMs, while lower contact angles may be indicative of defects or hydrophilic properties. Electrochemical techniques like cyclic voltammetry have been employed to study the electron transfer properties of SAMs on conductive substrates in certain

instances [44]. This yields very useful information about the density and orientation of functional groups that may influence electron transport processes. Some of these methods used in the study of this thesis will be explained in detail in Chapter 2. Combining multiple methods is essential to fully understanding a monolayer's structure, composition, and properties, which has important implications for the continued development and optimization of technologies based on these assemblies.

CHAPTER 2

EXPERIMENTAL

2.1 Materials and experimental procedures

The thiol-based compounds used to grow SAMs and the substrate of choices will be discussed in this section. Details of the cleaning procedures, as they possess a critical role, as well as the growth techniques will be listed.

2.1.1 Materials and reagents

In the pursuit of developing innovative materials, SAMs of carboranethiol molecules, including O1, O9, P1C, diMe-O9, mm-SH, and pp-SH, were mainly the focus of this thesis as they were detailed in Chapter 1. These materials, which have delicate synthesis processes, are not commercially available. They were synthesized in the Institute of Inorganic Chemistry of the Czech Academy of Sciences and they were provided by Dr. Tomáš Baše, within the scope of an international TÜBİTAK collaborative project. All of the carboranethiol molecules are known to have high purity, as they were characterized by nuclear magnetic resonance (NMR) spectroscopy and gas chromatography-mass spectrometry (GC/MS) in the Czech Academy of Sciences. They were stored under atmospheric conditions at 4°C in glass vials. They all have a whitish powder form, as seen in Figure 2.1.

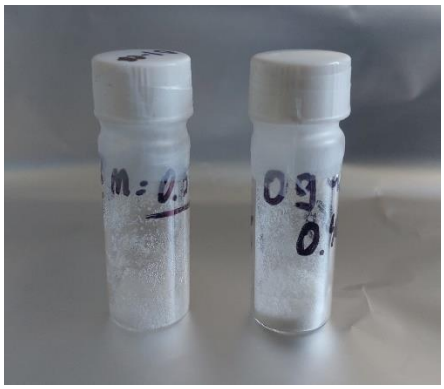

Figure 2.1. Glass vials containing O1 (left) and O9 (right) molecules.

The Turkish side has also participated in the synthesis of O1 in Prague. This synthesis involves adding a thiol group to pre-purchased o-carborane molecules. The synthesis procedure started with the pre-treatment of some chemicals: O-carborane and sulfur powder were dried on a rotary evaporator for several hours to remove possible moisture. Monoglyme (1,2-dimethoxyethane) was dried by refluxing over a mixture of Na and K in the presence of benzophenone and was freshly distilled before use.

The procedure then continued as follows: O-carborane (13.92 g) and sulfur powder (6.53 g) were added to the suspension of NaH (8.77 g, 60% in mineral oil) in ~200 mL of monoglyme in an inert atmosphere of nitrogen. The mixture was vigorously stirred for 6 hours at 65 °C. The color of the mixture first appeared reddish or brownish, but it turned yellow after 6 hours. Then, methanol (20 mL) was added to cool the mixture in a cold water bath. The volatile solvent was removed on a rotary evaporator under reduced pressure overnight. The residue (a yellow viscous mixture) was diluted with 100 mL of distilled water. The oily substance that appeared in the mixture of distilled water was easily removed by extraction into 25 mL of hexane. Hexane extraction was repeated five times. The water phase was then acidified with an aqueous solution of HCl (20 mL of 35% HCl and 30 mL of distilled water). Immediately, a white solid precipitated, and the originally yellow-clear solution (containing 1-SNa-1,2-$C_2B_{10}H_{11}$) turned into a white suspension. The mixture was extracted with 5 × 50 mL of hexane. The collected hexane phases were dried over

$MgSO_4$ for 2 hours and filtered. Then, the solvent (hexane) was evaporated in a rotary evaporator under reduced pressure.

The final product weighed 11.9 grams. ^{11}B NMR spectrum of the product was very similar to the ^{11}B NMR spectrum of O1 shown in the supporting information of the reference [54], so it can be said that the product is practically pure. ^{11}B NMR spectra of an O1 sample are shown in Figure 2.2. Chemical shifts are at locations -11.72, -13.02, -9.70, -9.70, -6.71, and -1.65, respectively, corresponding to molecular positions of 3-6, 4-5, 7-11, 8-10, 9, and 12.

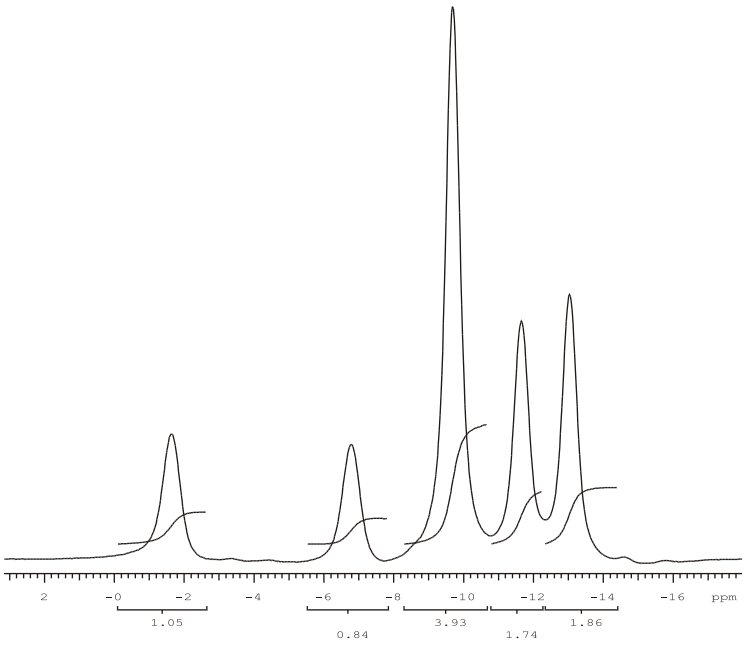

Figure 2.2. 1-(HS)-1,2-$C_2B_{10}H_{11}$ (O1): 1-D ^1H-decoupled ^{11}B NMR spectrum, retrieved from ref [54].

Most of the chemicals required for experiments and cleaning were purchased from ISOLAB (Turkish supplier) listed as ethanol (≥99.9%), acetone (≥99.5%), hydrochloric acid (37%), sulfuric acid (95-98%), hydrogen peroxide (35%), glycerol (99%), ethylene glycol (≥99.0%), dimethyl sulfoxide (≥99.9%), sodium hydroxide (≥99%). Some complementary experiments were done with 1-octadecanethiol (ODT), 1-decanethiol (DT), and 9-(HS)-1,7-$C_2B_{10}H_{11}$ (M9). ODT and DT were

purchased from Sigma-Aldrich, and M9 was purchased from Katchem. Ruby muscovite mica sheets (grade #1, V1/V2 Optical grade) used for the substrate preparation process were purchased from S&J Trading Inc. The Epoxy layer in the process was Norland Optical Adhesive 61 purchased from Optomek (Turkish distributor).

2.1.2 Preparation of substrates

Smooth gold surfaces were prepared using the template-stripping method [55], [56]. An atomically flat template is needed for this type of application. The deposition of gold on this template and then the separation of these gold and template layers is the crucial part. Mica sheets were chosen as templates for our studies. Freshly cleaved, atomically smooth mica sheets were placed inside the high-vacuum thermal evaporation chamber (base pressure $\leq 1 \times 10^{-6}$ Torr) for gold deposition. The deposition process was carried out using Vaksis MiDAS thermal evaporation systems at the UNAM (National Nanotechnology Research Center) facilities or Nanovak thermal evaporation systems at the GÜNAM (Center for Solar Energy Research and Applications) facilities. 0.5 grams of pure gold was used for an area of approximately 100 cm^2 of mica surface. Deposited gold had a thickness between 80 and 100 nm, sufficient for subsequent monolayer formation and characterization. Gold was deposited at a rate of 0.1 Å/s between 0 and 5 nm, 0.2 Å/s between 5 and 15 nm, and 0.3 Å/s after 15 nm of thickness.

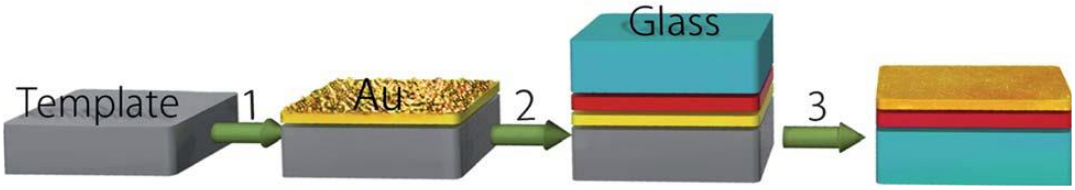

Figure 2.3. Schematic illustration of the template stripping process with gold surface. The smoothness difference between the thermally evaporated gold and template-stripped gold is depicted. Retrieved from ref [25].

After the deposition process was completed, the mica sheet with a gold layer was carefully cut into small strips. 1 cm to 1 cm glass wafers that were cleaned before the deposition were adhered to those strips with the help of Norland Optical Adhesive 61. UV cure is needed for this type of epoxy, so mica-gold-epoxy-glass interfaces were sandwiched between 2 square glass pieces, as shown in Figure 2.4, and they were put inside a UV chamber for 24 hours. Philips TL 8W BLB UV-A light source was used inside the chamber. These 2 glass pieces were held together with 2 plastic clamps. To minimize the pinholes and cracks on the gold surface, the force applied by those clamps was tweaked, but no significant effect of the force tweaking on the surface defects was observed. 1 cm to 1 cm of gold chips were ready to be stripped from the mica after the UV curing. Mica residues were observed on some of the template-stripped gold (TSAu) chips, making some of them unusable for monolayer studies. However, more than half of those chips had little to no mica residue on their surfaces. It is important to apply lateral force in the stripping process, which helps get surfaces with no residue.

The quality of TSAu surfaces was assessed using AFM. The average RMS roughness value of the Au(111) surfaces usually yields around 0.3 nm. Some nanoscale cracks or pinholes were observed on the surface. Future experiments confirmed that the effect of these defects was very minimal on the monolayer quality.

Figure 2.4. Glass wafers adhered to mica-gold strips, prepared for subsequent sandwiching between two glass pieces, and curing with UV light.

2.1.3 Formation of SAMs

Two different types of SAM deposition methods were used with the aim of getting surfaces with greater quality. Although the emphasis was on SAM grown from solution, vacuum deposition experiments were conducted as well. The experimental details of these two methods will be discussed in this section.

2.1.3.1 Solution-phase SAM growth

The deposition of monolayers from ethanolic solutions was mainly used in our studies. To achieve contaminant-free surfaces essential for SAM applications, all glassware, including glass vials used for preparing ethanolic solutions, was cleaned with piranha solution. The piranha solution, a mixture of concentrated sulfuric acid (H_2SO_4, 95–98%) and hydrogen peroxide (H_2O_2, 35%), was prepared in a 3:1 volume ratio, respectively [57]. The solution is highly corrosive and it reacts with organic materials, so the cleaning procedure was conducted in a fume head with appropriate personal protective equipment. The procedure requires a good pre-cleaning which was performed by rinsing the equipment with acetone and ethanol. Ultrasonic cleaner

and UV-OZONE cleaner were used to clean other laboratory equipment where piranha solution would not be applicable.

Ethanolic solutions of thiol-based molecules were prepared at a concentration of 1 mM. The preparation involved dissolving the calculated amount of thiol compound in absolute ethanol within the glass vials. Freshly prepared solutions were used prior to experiments to minimize the degradation of carboranethiol/alkanethiol molecules. TSAu chips, newly cleaved to expose Au(111) surfaces, were immersed in solutions with the help of metal tweezers. Samples were kept in the solution for 14-20 hours for highly ordered monolayer growth [7]. They were rinsed with ethanol and dried with a nitrogen stream after the growth phase to eliminate physisorbed molecules on the sample surface, then put in a sample holder for characterization. Samples were always handled using clean metal tweezers, and they were cleaned again with ethanol between characterizations with different methods. They were always kept in an inert atmosphere.

2.1.3.1 Vapor-phase growth

A technique called supersonic molecular beam deposition was employed for the vapor phase growth of carboranethiol SAMs. As mentioned in Chapter 1, SMBD is a very precise thin film growth technique, having huge advantages compared with conventional techniques of evaporation. This method allows better control of the nucleation and growth mechanism and fine-tuning of the properties of the film. In SMBD, two chambers make up the system: one chamber for the organic beam source (OBS) and another for the sample holder (SH), separated by a shutter in front of the skimmer. The organic molecules, like O9, are located in a quartz spoon inside the OBS chamber and evaporated with a spiral heater into a carrier gas, usually helium, argon, or krypton. This mixture of organic molecules and carrier gas undergoes supersonic expansion into a vacuum to form a molecular beam. The kinetic energy and flux of the beam can be controlled by adjusting source temperature, nozzle temperature, carrier gas used, and carrier gas inlet pressure.

A quartz crystal microbalance (QCM) and substrates are placed in the SH chamber mounted on a movable mechanism. It is used to measure the deposition rate before exposure to the beam. Film growth is allowed to continue to attain the desired thickness, usually as estimated by deposition time. The dimensions or uniformity of the film can be tailored by changing parameters such as skimmer-sample holder distance in order to obtain a Gaussian shape with a central homogeneous zone [58].

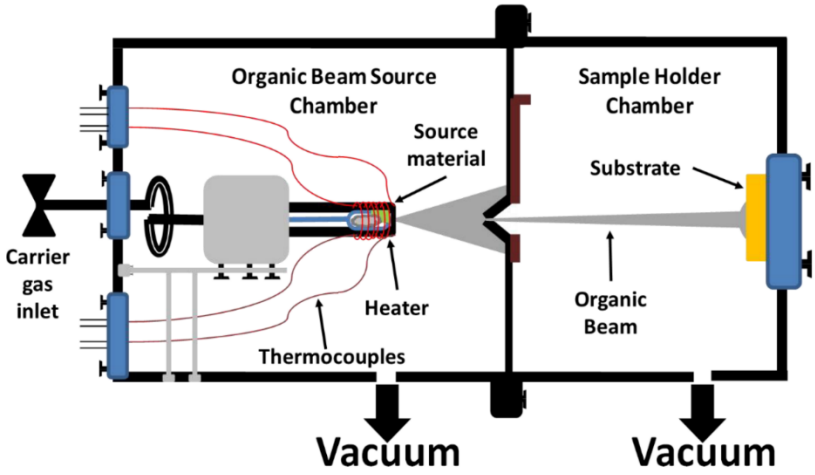

Figure 2.5. Schematic representation of the SMBD chambers. The source material is evaporated using a heater, with the temperature monitored via thermocouples. The resulting organic beam passes through a skimmer before being directed onto the substrate. Retrieved from ref [58].

The vacuum levels of the two chambers are maintained using a combination of vacuum pumps. Each chamber is equipped with rotary and booster pumps to achieve an initial rough vacuum level. Subsequently, diffusion pumps are activated to attain high vacuum levels. Prior to the start of the deposition process, the vapor pressure in the OBS chamber is typically between 2×10^{-7} Torr and 5×10^{-7} Torr, while the pressure in the SH chamber is reduced to 1×10^{-6} Torr to 2×10^{-6} Torr. These pressure levels are more than adequate for most vacuum deposition techniques [59].

Helium was selected as the carrier gas for the process. A vacuum gauge is installed on the gas inlet, where the inlet pressure is maintained at -0.4 bar, as indicated by the gauge, corresponding to 0.4 bar below atmospheric pressure. During the procedure, the nozzle is initially heated to prevent clogging, followed by heating the source material to the desired temperature. Once stable temperatures are achieved, the shutter is opened, and the beam is directed onto the QCM to measure the deposition rate. When the desired deposition rate is obtained, the shutter is temporarily closed, and the sample is aligned with the skimmer using a movable sample selection wheel. Deposition begins when the shutter is reopened. Deposition times typically range from 10 to 60 minutes, depending on the sample requirements. The SMBD system employed in this study was initially deconstructed at the beginning of this research. Subsequently, it was reconstructed with extensive optimizations and adjustments. As a result, the experiments conducted with the system were limited by these factors.

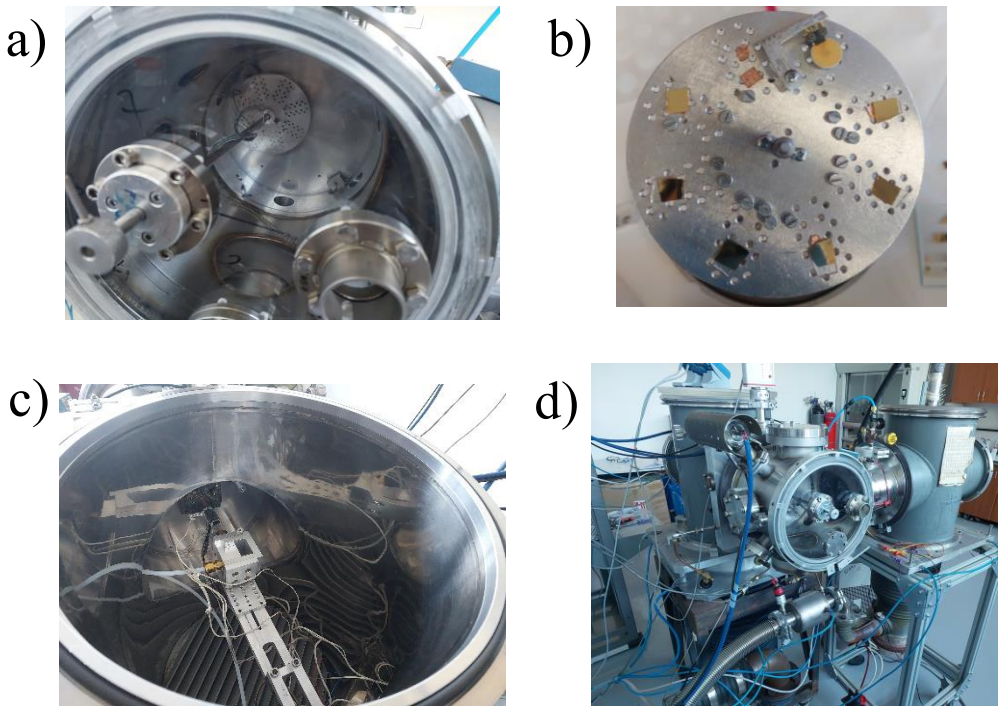

Figure 2.6. Pictures of the SMBD system, showing (a) SH chamber, (b) SH movable wheel with QCM crystal and 6 gold substrates, (c) OBS chamber, (d) overall view of SMBD system.

2.2 Characterization techniques

2.2.1 Atomic force microscopy

Atomic force microscopy (AFM) has been a powerful characterization technique in surface sciences since its invention in 1985. It primarily acts as a tool to map surface topography in atomic or near-atomic resolutions. In contrast to optical microscopy techniques, depending on the diffraction limit of light, AFM works by physically probing the surface and hence can attain much higher resolution. The basic principle of operating an AFM depends on a sharp tip mounted on a flexible cantilever. Since the tip scans over the sample surface, it undergoes some forces due to interactions with atoms of the sample. These forces cause minute deflections in the cantilever, which are usually detected and measured. A laser beam is commonly focused on the back of the cantilever and reflected into a position-sensitive photodetector. Changes in the deflection of the cantilever result in changes in the position of a reflected laser spot on the detector, allowing very precise measurement of the cantilever's movements. A visual depiction of AFM can be seen in Figure 2.7.

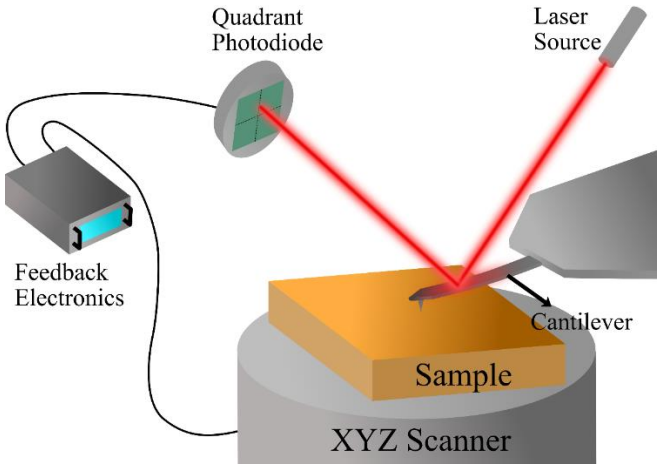

Figure 2.7. Visual depiction of AFM measurement setup. The bending of the cantilever is detected via a laser and a photodiode. Depending on the feedback, the XYZ scanner adjusts the vertical position of the sample.

There are a wide variety of cantilevers to choose from depending on the mode of operation and the sample. They can be characterized by their spring constants, and cantilever deflection is converted into force using Hooke's Law. The spring constant is calculated as in Equation 4, where E is the Young's modulus (stiffness measure). Cantilevers' dimensions are denoted as w, t, and l.

$$k = \frac{Ewt^3}{4l^3} \tag{4}$$

Typical values of k range between 0.1 N/m to 100 N/m; however cantilevers with much larger stiffness are present, generally used for nanoindentation purposes [60]. Quality factor and eigenfrequency are important parameters in AFM characterization, as they influence the sensitivity and performance of the cantilever. Quality factor (Q) is a dimensionless parameter characterizing energy loss concerning the energy stored in the oscillating system. A higher value of Q corresponds to lower energy dissipation, which means that the cantilever is more sensitive to weak forces. The quality factor becomes very important in dynamic modes of AFM, for example, tapping mode or non-contact mode, when the cantilever oscillates near its resonance frequency.

The eigenfrequency (f_0), sometimes also called the natural resonance frequency of the cantilever is dependent on its physical dimensions, material properties, and spring constant, given by the relation [61]:

$$f_0 = \frac{1}{2\pi}\left(\frac{k}{m_0}\right)^{\frac{1}{2}} \tag{5}$$

k in the Equation 5 is the spring constant, m_0 is the mass of the cantilever. Operating close to the eigenfrequency in the dynamic modes increases the sensitivity of the cantilever because minute forces will strongly vary in oscillation amplitude or phase.

AFM has a number of different operating modes, each specialized for particular applications and types of samples [62], [63]. In contact mode, during scanning, the AFM tip is kept in continuous contact with the sample surface. This mode allows

high-resolution topographical and frictional measurements. However, in this mode, the tip is in direct contact with the surface, and therefore lateral forces can be exerted, which might be harmful for soft or fragile samples. In order to overcome this limitation, tapping mode introduces a dynamic approach where the cantilever oscillates near its eigenfrequency. During operation, the tip intermittently touches the surface, thereby minimizing lateral forces while high-resolution imaging is maintained. This makes the tapping mode especially suitable for imaging soft or adhesive materials. Another operational approach is the non-contact mode, in which the cantilever only slightly oscillates above the sample surface without touching it. Instead, it detects long-range forces such as van der Waals or electrostatic interactions. The non-contact mode is mainly used for very soft and fragile samples since this mode provides no mechanical disturbance to the surface.

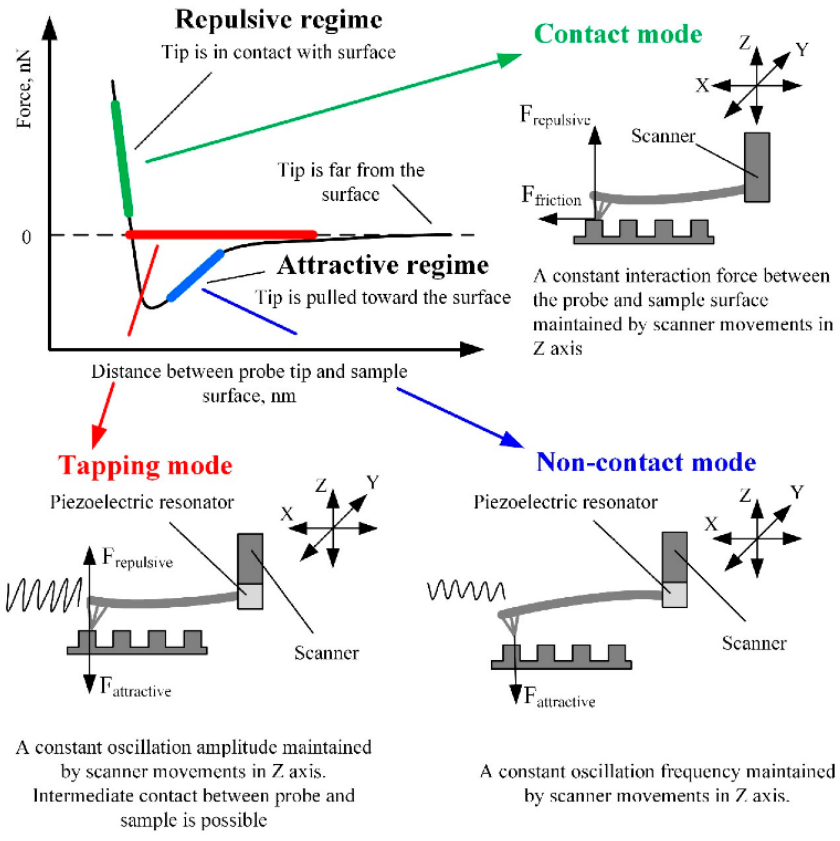

Figure 2.8. AFM working modes in respect of Van der Waals force. Retrieved from ref [62].

In the studies of this thesis, the Nanomagnetics Ambient Scanning Probe Microscope (SPM) was utilized for nanoscale surface characterization. Measurements were conducted using Bruker NCHV-A probes operating in tapping mode with a resonance frequency of 320 kHz. These antimony-doped silicon probes feature a force constant of 42 N/m, and a tip radius of 8 nm.

2.2.2 Contact angle measurements

Contact angle (CA) goniometry is a technique in the measurement of wetting properties of a surface by determining the contact angle formed where a liquid droplet meets a solid surface. Wetting refers to the study of examining the macroscopic effects of intermolecular interactions between liquids and solids in contact, with the contact angle providing a measure of the surface's hydrophobicity or hydrophilicity [64]. The measurement involves depositing a liquid droplet on the surface, after which its profile is viewed by a camera. Consequently, the CA can be calculated with reference to the angle at the liquid-solid-air interface, from where the information about surface energy and interfacial interaction is derived.

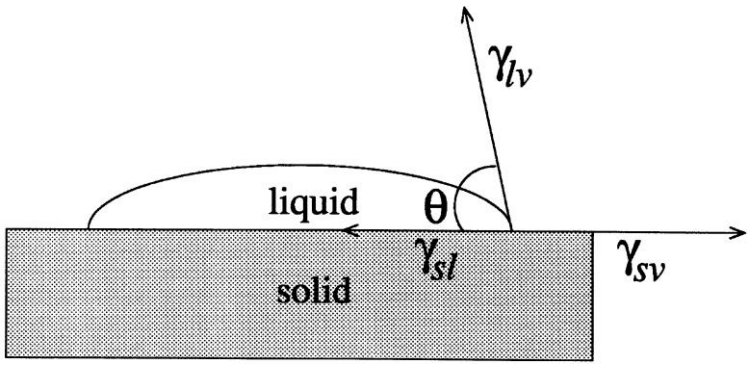

Figure 2.9. Schematic of a sessile-drop contact angle system. Retrieved from ref [53].

Young's equation (Equation 6), which was postulated back in 1805, describes the CA since it states the equilibrium for the corresponding interfacial tensions. Young's equation relates this contact angle, θ_Y, with the tensions of the respective solid-vapor,

γ_{sv}, solid-liquid, γ_{sl}, and liquid-vapor, γ_{lv}, interfacial tensions, providing a theoretical framework when interpreting these surface interactions.

$$\gamma_{lv}cos\theta_Y = \gamma_{sv} - \gamma_{sl} \quad (6)$$

The static, advancing, and receding contact angles define the three-phase contact line in terms of the interaction a liquid makes with a solid surface [65]. The static CA refers to the equilibrium angle that would be formed by a droplet due to the balance of surface tensions at the solid-liquid-vapor interface given by Young's equation. The advancing contact angle is the angle at which the droplet expands or tilts forward, representing the maximum angle before the contact line moves outward. The receding contact angle is observed when the droplet contracts or tilts backward, showing the minimum angle before the contact line retracts.

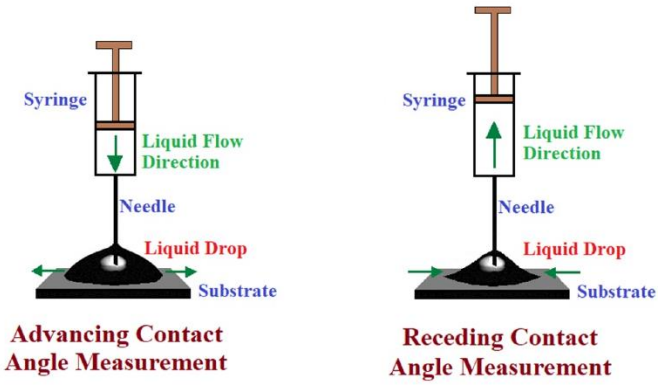

Figure 2.10. Schematics of advancing and receding contact angles. Retrieved from ref [65].

The ease of contact angle measurements on suitably prepared solid surfaces is one of the reasons the technique has seen such wide usage, but this apparent simplicity conceals the complexity involved in ensuring accurate and meaningful measurements. Features present in most real-world surfaces include roughness and chemical heterogeneity that may affect contact angles very strongly. Such surface imperfections often lead to contact angle hysteresis described by the difference between the advancing and receding angles. In such cases, the experimentally observed contact angle may well deviate from the theoretical equilibrium angle

defined by Young's equation, complicating the interpretation of the results [53]. Moreover, surface roughness, when present, often gives measured angles that reflect the topography of the surface rather than the intrinsic surface energetics and hence are inapplicable directly within Young's framework. Another cause of variability within the measurement of contact angle is experimental techniques. Goniometer methods, in their usual format, although being widely applied, are subjective and of low precision. Newly developed methodologies, which aim at overcoming the above-mentioned disadvantages, include Axisymmetric Drop Shape Analysis, widely known as ADSA. Automation of measurements with higher accuracy provides the possibility of improved dynamic contact angle behavior. Despite these challenges, contact angle goniometry remains a valuable method of investigating surface properties, providing measurements are conducted with due regard for surface preparation and experimental design. This thesis discusses the principles and methodologies of contact angle goniometry, with specific emphasis on factors affecting the reliability of the technique.

Young’s equation alone isn’t enough to determine the solid-vapor surface tension because the solid-liquid surface tension is unknown. To address this, researchers have developed interpretation models that use contact angle data from multiple liquids with known surface tension properties. Some of the most well-known models [53], [66] include Zisman’s Critical Surface Tension, which identifies the critical surface tension at which a liquid just wets a solid, providing an estimate of the solid-vapor surface tension. The Owens-Wendt (and Wu) models break surface tension into dispersive and polar components, using mathematical approximations to determine the solid’s contribution. The van Oss-Chaudhury-Good (vOCG) model builds on Fowkes’ theory by adding acid-base interactions alongside Lifshitz-van der Waals forces, offering a more detailed perspective on surface interactions. Neumann’s Equation of State takes a different approach, directly linking solid-liquid surface tension to solid-vapor and liquid-vapor surface tensions through an empirical equation, eliminating the need to separate components. Each model makes specific assumptions about molecular interactions, which means they work better for some

systems than others. Classical surface tension component approaches (e.g., Fowkes, Owens-Wendt), which attribute solid surface tension to contributions from distinct intermolecular forces (e.g., dispersive, polar), were criticized by Neumann [67], [68]. He advocates for an equation-of-state approach, treating solid surface tension as a constant material property. Building on Berthelot's combining rule for molecular interactions, a modified equation-of-state relation can be derived as:

$$\gamma_{sl} = \gamma_{lv} + \gamma_{sv} - 2\sqrt{\gamma_{lv}\gamma_{sv}}\, e^{-\beta(\gamma_{lv}-\gamma_{sv})^2} \tag{7}$$

Combining Eq. (7) with Young's Eq. (6) yields:

$$cos\theta_Y = -1 + 2\sqrt{\frac{\gamma_{sv}}{\gamma_{lv}}}\, e^{-\beta(\gamma_{lv}-\gamma_{sv})^2} \tag{8}$$

β is an empirical constant, and if its value is known, solid surface tension can be experimentally determined using liquid surface tension and contact angle data, which can be measured. From the experimental contact angle on different surfaces, an average value of β is obtained as 0.0001247 $(m^2/mJ)^2$ [67]. The method is experimentally verified, and it offers practical advantages such as predicting wettability from minimal data.

In the studies of this thesis, CA measurements were recorded using Attention Theta Optical Tensiometer. Both static and dynamic CAs were measured. A separate motorized syringe system was utilized for dynamic CA measurements. A glass syringe was attached to the motorized syringe. The tubing used in the setup is made from polyethylene, while the syringe tip and fittings are made of polypropylene. Those materials were chosen to be compatible with the DI water and other chemicals used for the CA measurements. Four different syringe-tube-needle systems were prepared for four different chemicals used for CA experiments, which ensures that there will be no cross-contamination between the chemicals. Dynamic CA measurements were taken at a rate of 25 µL/min. Deionized (DI) water (18.2 MΩ.cm) was used for the measurements. For each sample, three different spots were measured to get an average. 10 images were recorded for each spot with 304 ms time

intervals, making them 30 in total for successive static, advancing, and receding measurements. The sample stage was leveled using a level gauge before each set of measurements. Room temperature was monitored in each session to match 25°C. The drop volume was chosen to be ~4 μL. Static CA snapshots were recorded as soon as the drop contacted the surface.

2.2.3 Spectroscopic ellipsometry

Spectroscopic ellipsometry represents a powerful, nondestructive optical characterization method for investigating optical properties and the thickness of thin films and multilayer structures. It involves measuring changes in the polarization state of light as reflected or transmitted by a material system. Consequently, a great amount of detailed information may be retrieved with high accuracy concerning the complex refractive index, dielectric function, and layer thickness of materials [69]. Ellipsometry depends on the principle of the interaction between polarized light and a sample surface. It is either linearly polarized or elliptically polarized and hits the sample in an oblique manner. Because of the interaction that will follow, the reflected or transmitted material is in another polarization state. The variation in polarization state, known as the complex reflectance ratio, is denoted as:

$$\rho = \frac{R_p}{R_s} = \tan\Psi e^{i\Delta} \tag{9}$$

R_p and R_s are the complex Fresnel reflection coefficients for p-polarized and s-polarized light, respectively. The parameters Ψ and Δ are the amplitude ratio and phase difference between the p and s-polarized light components, respectively. These are the primary quantities that are measured in spectroscopic ellipsometry.

Spectroscopic ellipsometry involves optical modeling in analysis, within the ellipsometric data framework concerning material stack but also eventual anisotropy, roughness, or inhomogeneity. Because experimental data fit into theoretical models, a high degree of accuracy can be ensured in determining the structural and optical

properties of the sample. Hence, spectroscopic ellipsometry is applied in semiconductor research, thin-film coatings, and nanotechnology that demand very precise material characterizations.

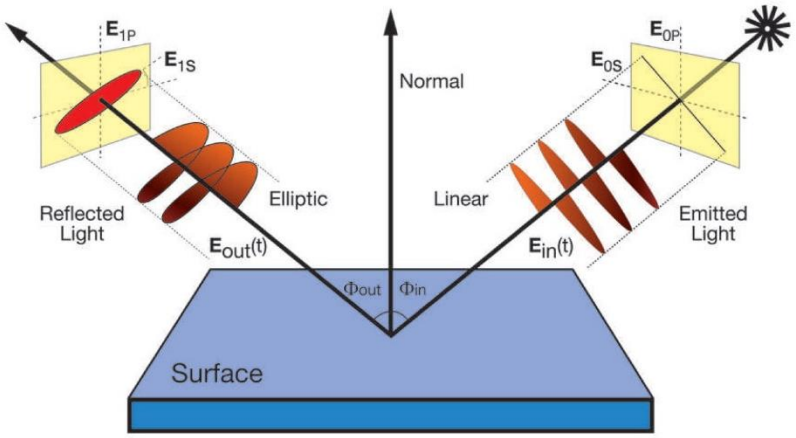

Figure 2.11. Representation of ellipsometry: linearly polarized incident light reflects off a surface, becoming elliptically polarized. Retrieved from ref [70].

Thickness measurements of the monolayer are a direct indication of the presence of the monolayer. However, due to the expected thickness being extremely small for carboranethiol SAMs, very precise instrumentation is needed. For this purpose, a JA Woollam V-Vase Ellipsometer was utilized. All the measurements were taken between the spectral range of 400 nm and 1100 nm. The incidence angle was chosen to be 65°. Reference measurements of the gold substrates were taken before measuring the monolayer thickness. The Cauchy dispersion model was used to fit the monolayer on top of reference TSAu data. Delta values obtained from the measurement were used to model the monolayer. In Figure 2.12, delta values of the reference TSAu and O1 monolayer on top are shown, which are well-aligned with the literature [71]. The subtle difference between those allows us to obtain monolayer thickness.

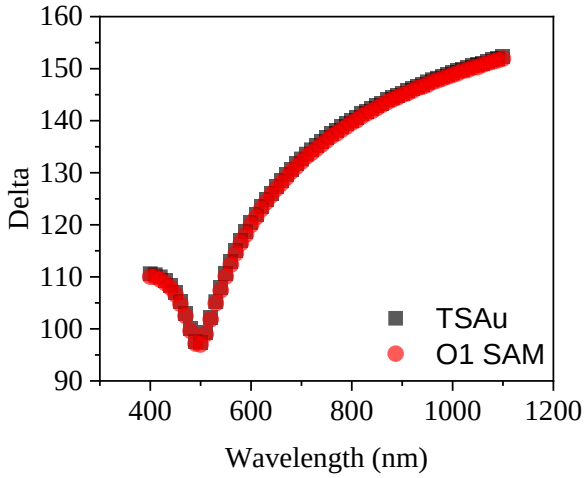

Figure 2.12. Delta values across different wavelengths of TSAu substrate and O1 monolayer.

2.2.4 X-ray photoelectron spectroscopy

X-ray photoelectron spectroscopy (XPS), also called ESCA, is a well-known analytical technique of surface chemistry investigation of materials [72]. It gives detailed quantitative information on the elemental composition, the chemical states, and the electronic environment of the atoms constituting the topmost atomic layers (up to a depth of about 5-10 nm). The surface sensitivity arises from the limited inelastic mean free path of the emitted photoelectrons in solid matter. The fundamental principle of XPS is based on the photoelectric effect [73], as described by Einstein's equation:

$$E_k = hv - E_b - \phi \tag{10}$$

E_k is the kinetic energy of the emitted photoelectron, hv represents the energy of the incident X-rays. E_b is the binding energy of the electron relative to the Fermi level, and ϕ denotes the work function of the spectrometer. It is possible to measure the kinetic energy of photoelectrons and find the binding energy of electrons in some particular atomic orbital.

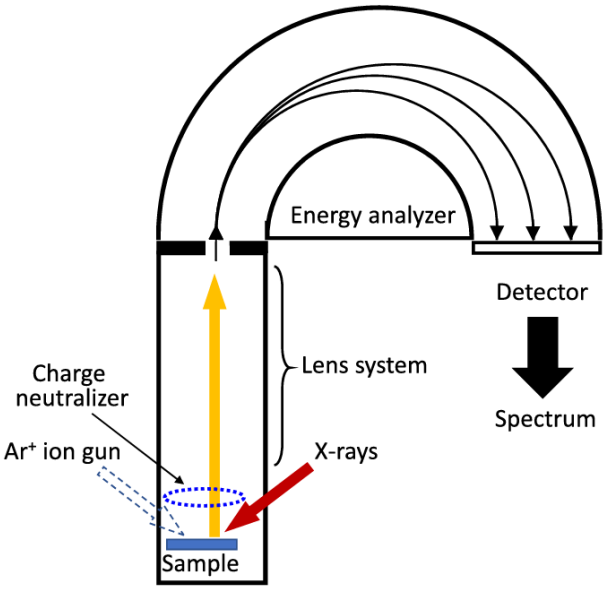

Figure 2.13. The diagram of the photoelectron spectrometer featuring a hemispherical electron energy analyzer. Retrieved from ref [73].

The binding energy is a characteristic of each element but is modified by the local chemical environment, including the oxidation state and bonding configuration. This makes XPS highly effective for chemical state analysis: for example, a shift in binding energy, or chemical shift, can indicate changes in electron density around the atom that are diagnostic of specific functional groups or oxidation states. XPS would be performed classically by exposing the surface of a material to a focused X-ray beam and collecting the emitted photoelectrons by means of an electron energy analyzer. In the resulting spectrum, there are peaks related to the core-level binding energies of the elements present. Quantitative analysis can be obtained by considering the peak areas, normalized by sensitivity factors of each element.

Apart from elemental and chemical state analysis, XPS can also yield information regarding the relative surface concentration of elements. This is determined using the following equation:

$$C_i = \frac{\frac{I_i}{S_i}}{\sum_j \frac{I_j}{S_j}} \tag{11}$$

C_i is the atomic concentration of the element i, I_i represents the intensity of the photoelectron peak, and S_i is the sensitivity factor for the element i. The summation is performed over all detected elements.

The XPS device available at the UNAM (National Nanotechnology Research Center) facilities was utilized to acquire XPS spectra for this study. Both survey spectra and high-resolution scans were performed to ensure a comprehensive analysis of the sample's surface chemistry. High-resolution spectra were specifically obtained for the Au 4f, C 1s, B 1s, O 1s, and S 2p peaks, enabling detailed characterization of the chemical states and bonding environments of these elements.

CHAPTER 3

RESULTS AND DISCUSSION

3.1 Preliminary experiments

This thesis primarily focuses on the characterization with contact angle goniometry. Some preliminary experiments were performed to optimize the CA test setup. The effect of drop size on the CA is well-established in the literature [74], [75]. CA is expected to steadily decrease with the increasing drop size, which indicates that liquid drop size must be kept constant across all the measurements, especially if one wants to make a comparative study across different surfaces. We tested the drop size effect on the CA with M9 SAM surfaces. A representative data is shown in Figure 3.1. A general trend of decrease in CAs was observed with the increasing drop size; however, some random noise were still present. The observed noise in the measurements could potentially arise from factors such as surface heterogeneities or minor variations in drop deposition techniques. CA measurements are highly sensitive to environmental conditions and measurement techniques; therefore, attention must be given to ensure reproducibility. Another important factor that needs to be tested is the pumping rate of dynamic CAs. No significant change was expected with the variations in the pumping rate [76]. By increasing the rate from 5 to 35 µL/min, in increments of 5 µL/min, a 2.5° increase in advancing CAs was observed, as shown in Figure 3.2. Although the difference across the whole range is to a lesser extent, it is important to keep the pumping range constant. For future experiments, a pumping rate of 20 µL/min and a drop size of 4 µL were chosen to achieve more controlled conditions.

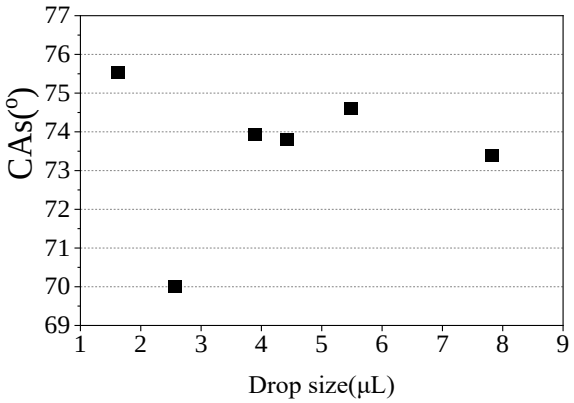

Figure 3.1. CAs of an M9 surface were plotted against the drop size, with measurements taken at the same spot on the sample.

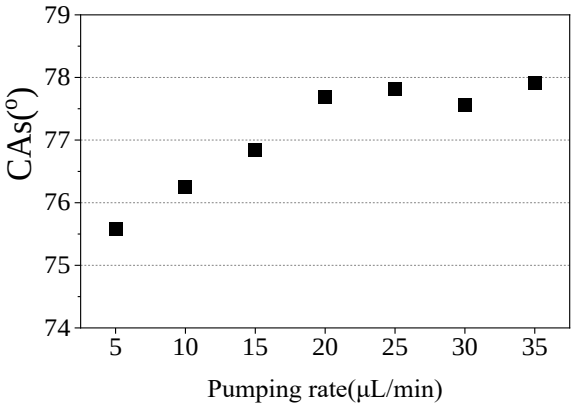

Figure 3.2. Pumping rate dependency of advancing CAs measured at the same spot.

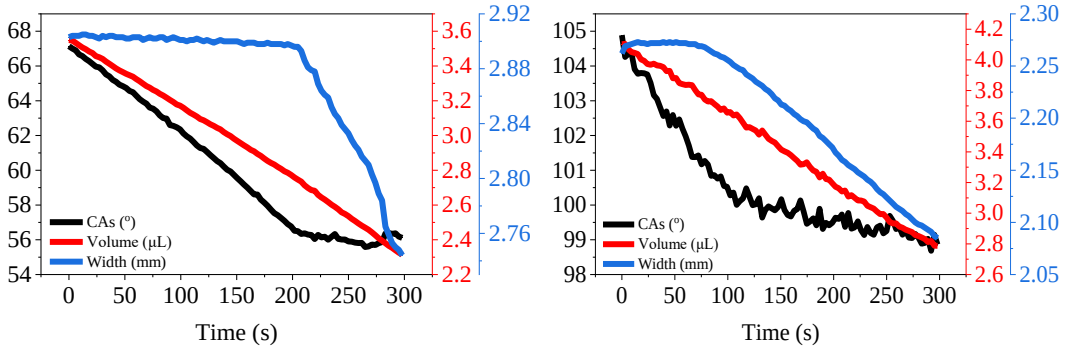

Figure 3.3. CAs, volume, and horizontal width of the drops are plotted for an M9 sample (left) and a DT sample (right).

Some experiments were performed with M9 and DT surfaces to observe the effects of the evaporation of the drop over time on the surface. Static CAs of DI water drops were recorded for 300 seconds with 3-second time intervals. CA, volume of the drop, and horizontal width of the drop were plotted over time for two representative M9 and DT surfaces in Figure 3.3. A more linear decrease with M9 surfaces was observed compared to DT surfaces. With the decreasing volume, the width of the drop initially stayed the same for the M9 sample, which directly resulted in decreasing CA. After some time, the width of the drop started to decrease, and CA stayed the same. We observed a similar behavior in the DT surface; the decrease in CA became slower after the width started to decrease. These behaviors were observed in the other experiments and might indicate inhomogeneities on the surface, so one must be careful when measuring static CA. It must be measured immediately when the drop contacts the surface. These preliminary experiments underline the necessity of standardizing experimental parameters, such as drop size and pumping rate, that will provide reliable measurements of the CA. The noise observed in drop size experiments, as shown in Figure 3.1, suggests that even minor differences in experimental conditions can lead to inconsistencies, again emphasizing the stringency of protocol adherence. Contributing factors are likely to involve surface heterogeneity and deposition technique variability; further surface characterization is required to correlate these with the deviations in CA.

In general, SAM surfaces were washed with ethanol before characterization to remove physisorbed molecules. It was observed that washing pure substrates also significantly affects CAs, as seen in Figure 3.4. No differences in monolayer quality were observed depending on whether the substrates were washed prior to immersion. Nevertheless, all substrates were washed in subsequent experiments. This raises the question: “What value of CA should be chosen as a reference?” Although this question has no definitive answer, some experiments were conducted to gain a better understanding of the surface properties of Au(111) substrates.

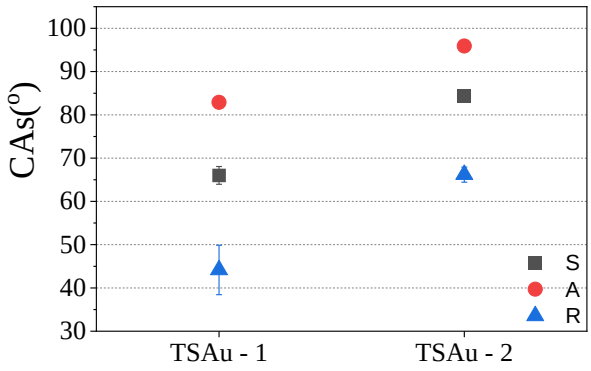

Figure 3.4. CAs of two TSAu substrates after they are freshly cleaved from mica. The second one was rinsed with ethanol, whereas the first one was not. S, A, and R in the graph refer to Static, Advancing, and Receding CAs.

Another question that will be important is "Whether air exposure significantly change CAs?" To better understand the topic, the following experiments were conducted: 5 gold substrates were stripped at the same time, and their CAs were sequentially measured. Although samples were inside containers, they were kept in touch with air; no inert atmosphere was present. We saw an increase in CAs with each substrate. There were ~15 minutes between the measurements of each substrate, but the first one was measured directly after stripping. Longer exposure times to the air further increased the contact angle. These results can be seen in Figure 3.5. Receding measurements completely wetted the surface, so they are not present in the graph. The increase in CAs is attributable to the contamination of surfaces when they are exposed to air. This data and unrepresented results show that static CA is saturated around 70 degrees over time. To test the effect of ethanol washing on substrates, 5 of them were stripped and rinsed with ethanol with the help of a wash bottle (Substrates 6-10 in Figure 3.5). Rinsing took 10 seconds, using ~8 mL of ethanol for each sample. Although all the samples were sequentially measured with ~15-minute time intervals, we got very consistent CAs. Substrates were labeled as TSAu 6 to 10 to avoid confusion with the previous measurements.

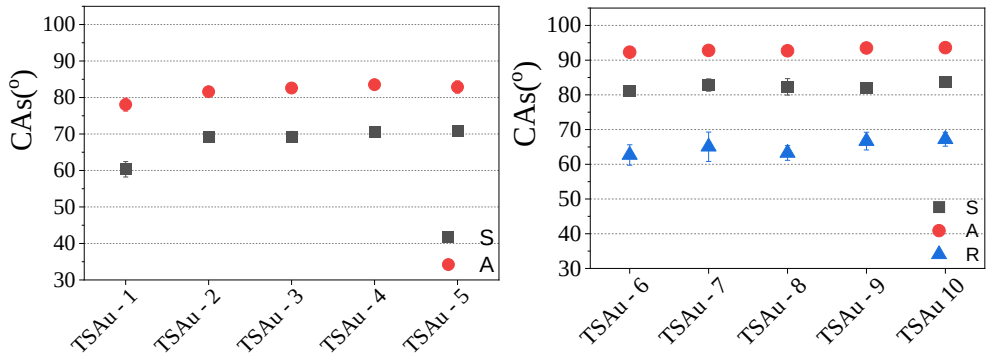

Figure 3.5. Contact angles (CAs) were sequentially measured on 10 TSAu substrates. Substrates 1–5 were not rinsed with ethanol, whereas substrates 6–10 were rinsed. There was approximately a 15-minute interval between each measurement, but all substrates (1–5 and 6–10) were stripped at the same time. Substrates 1 and 6 were measured immediately after stripping.

Stable values obtained in the CAs of substrates washed with ethanol create a good reference point. Ethanol rinsing removes not only potential surface contaminants but also seems to stabilize the CA of the substrate, thus being a crucial step in the preparation protocol. To see if SAMs of carboranethiols are present and ordered on the surface, we can compare these results with the CAs of monolayers.

Additionally, to see whether taking reference CA measurements affects the monolayer quality, different types of substrates were immersed in solutions of O1 and O9. In Figure 3.6, 4 different SAM surfaces of O1 and O9 can be seen. Reference substrate measurements were taken for samples O1 - 1 and O9 - 1. However, substrates of O1 - 2 and O9 - 2 were directly immersed in solutions immediately after being cleaved. There was no significant difference between the SAMs of these two types of substrates.

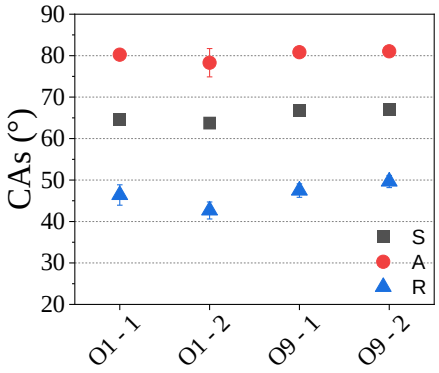

Figure 3.6. CAs of O1 and O9 samples. Reference measurements were performed on substrates for samples O1 -1 and O9 - 1. In contrast, the substrates of O1 - 2 and O9 - 2 were directly immersed in solutions immediately after cleaving.

This indicates that the process of taking reference CA measurements does not significantly alter the quality or uniformity of the resulting SAMs. The contact angle measurements for both O1 and O9, regardless of the pre-measurement process, which includes exposure to atmospheric conditions and water droplets, fell within a comparable range.

3.2 Ortho carboranethiol SAMs

In this section, O1 and O9 surfaces were characterized by conducting various experiments. Au(111) surfaces were the substrates of choice. The comparison of these two SAMs is crucial for a better understanding of molecular structures. The main idea behind this comparison is to see the stability of the surfaces and to see which one of these two isomers will be preferred on the gold surface.

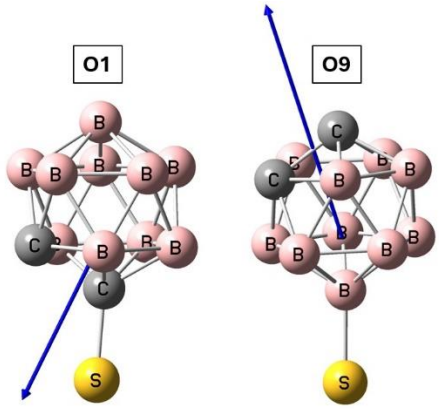

Figure 3.7. Molecular structures of O1 and O9 isomers (Hydrogens are omitted). Blue arrows represent their dipole moments.

This thesis will mainly report a comparative study of several isomers of carboranethiol. In general, however, most effort was dedicated to pure isomer characterization: because of the scarce amount of data available in literature. Two different methods of SAM preparation were tested: growth from solutions in base-free conditions and growth in basic conditions. The main difference between these two methods comes down to pH and the presence of NaOH. In solution, thiol groups (-SH) can lose a proton, turning into thiolate anions ($-S^-$), which help form monolayers on metal surfaces. Adding NaOH increases the pH, making this process easier and more efficient. That's why we call these "basic solutions"—they encourage thiol deprotonation, leading to a higher concentration of reactive thiolates. In contrast, "base-free solutions" don't have extra NaOH added, while they aren't necessarily pH-neutral. This means thiol deprotonation happens to a lesser extent, depending on the natural properties of the solvent. To examine these effects, two sets of O1 and O9 solutions were prepared using these carboranethiols (CTs). The exact amounts of molecules added to the ethanolic solutions and their measured pH values can be found in Tables 3.1 and 3.2. SAMs grown under base-free conditions are referred to as O1 and O9 (without additional modifiers), whereas those grown under basic conditions are labeled with a "-B" suffix (e.g., O1B, O9B) to denote the use of NaOH.

Table 3.1 Amount of molecules added to the base-free and basic solutions of O1 and O9 and pH values of these solutions from set 1.

	Volume	Amount of O1/O9	Molarity of O1/O9	Amount of NaOH	Molarity of NaOH	pH
O1	25 mL	4.4 mg	1.0 mM	-	-	4.45
O9	25 mL	4.4 mg	1.0 mM	-	-	5.54
O1 Basic	25 mL	4.8 mg	1.1 mM	1.2 mg	1.2 mM	8.32
O9 Basic	25 mL	4.3 mg	1.0 mM	1.0 mg	1.0 mM	7.91

Table 3.2 Amount of molecules added to the base-free and basic solutions of O1 and O9 and pH values of these solutions from set 2.

	Volume	Amount of O1/O9	Molarity of O1/O9	Amount of NaOH	Molarity of NaOH	pH
O1	25 mL	4.4 mg	1.0 mM	-	-	4.22
O9	25 mL	4.3 mg	1.0 mM	-	-	5.63
O1 Basic	25 mL	4.5 mg	1.0 mM	1.2 mg	1.2 mM	7.95
O9 Basic	25 mL	4.5 mg	1.0 mM	1.3 mg	1.3 mM	8.56

These pH measurements reveal the acidic nature of these CT isomers. The addition of NaOH neutralizes H^+ ions resulting from thiolate formation and shifts the solution to a slightly basic state. We expected samples prepared in basic solutions to have more stable SAMs.

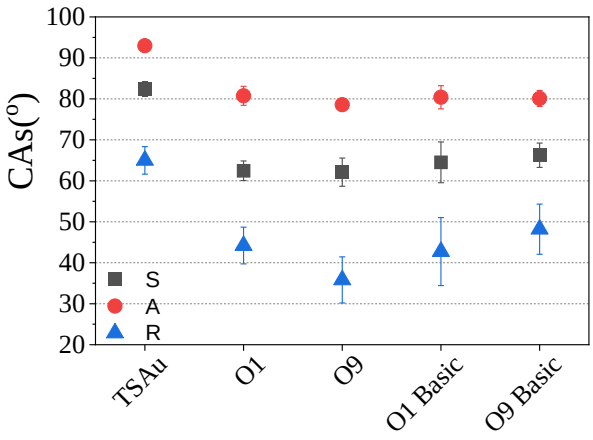

Figure 3.8. Averages of all CA measurements for O1 and O9 prepared in base-free and basic conditions. SAMs grown in base-free conditions are referred as O1 and O9. Average CAs of TSAu chips that are washed with ethanol are added for reference.

Table 3.3 The numerical values of the data points shown in Figure 3.8.

	S	**A**	**R**	**Δ**
TSAu	82.4 ± 1.8	93.0 ± 1.0	65.0 ± 3.4	28.0
O1	62.5 ± 2.4	80.7 ± 2.3	44.2 ± 4.5	36.5
O9	62.1 ± 3.4	78.6 ± 1.4	35.8 ± 5.6	42.8
O1 Basic	64.5 ± 5.0	80.4 ± 2.8	42.7 ± 8.3	37.7
O9 Basic	66.2 ± 3.0	80.1 ± 1.9	48.2 ± 6.1	31.9

Figure 3.8 shows averages of all CA measurements for O1 and O9 prepared in base-free and basic conditions with the addition of reference TSAu data. The reported values represent averages from four independent samples each of O1 and O9 under base-free conditions, and seven samples each under basic conditions. Reference TSAu data is the average of 5 samples. There is little difference observed between the samples prepared under base-free conditions and those prepared under basic conditions. Additionally, the contact angles (CAs) of O1 and O9 are very similar. This makes it harder to compare using CA goniometry. The drop in CAs of SAMs

compared to the substrates speculatively indicates monolayer formation. Characterization with different methods is needed to confirm that. Spectroscopic ellipsometry results can be seen in Figure 3.9. O1 and O9 monolayer thicknesses were in the expected range. The theoretical maximum thickness is ~0.85 nm for those SAMs. The slight bending of carborane structures, the presence of domain boundaries, or the formation of vacancy islands might explain why the maximum thickness was not observed. Since the spot size is in the order of millimeters in SE, higher values of thickness might indicate more ordered monolayers.

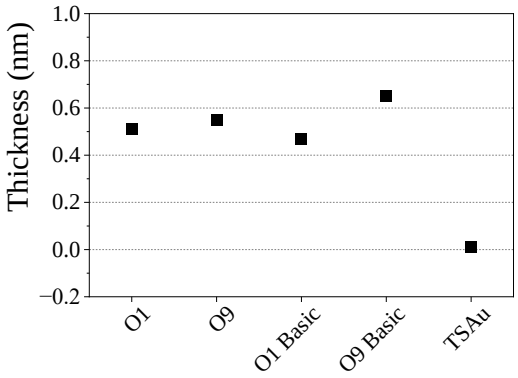

Figure 3.9. Thickness values of O1 and O9 samples prepared using solutions with base-free and basic conditions, obtained using spectroscopic ellipsometry. TSAu substrate is also added for reference.

Table 3.4. The numerical values of the data points shown in Figure 3.9.

	Thickness (nm)
O1	0.51
O9	0.55
O1 Basic	0.47
O9 Basic	0.65
TSAu	0.01

AFM characterization of O1 and O9 samples is important mainly because it lets us track if there are any defects or contamination on the surface. AFM images of TSAu

substrates and O1 and O9 samples can be seen in Figure 3.10. AFM images were captured in tapping mode, ensuring minimal disturbance of SAMs. There was no noticeable difference observed between the AFM images of TSAu and the images of O1/O9 SAMs. However, in general, O1/O9 SAMs yield slightly higher values of RMS roughnesses indicating monolayer presence on the surface. These results align with the conclusion drawn from CA measurements and spectroscopic ellipsometry. Further investigation with XPS could provide an additional understanding of the chemical composition and binding characteristics of these SAMs.

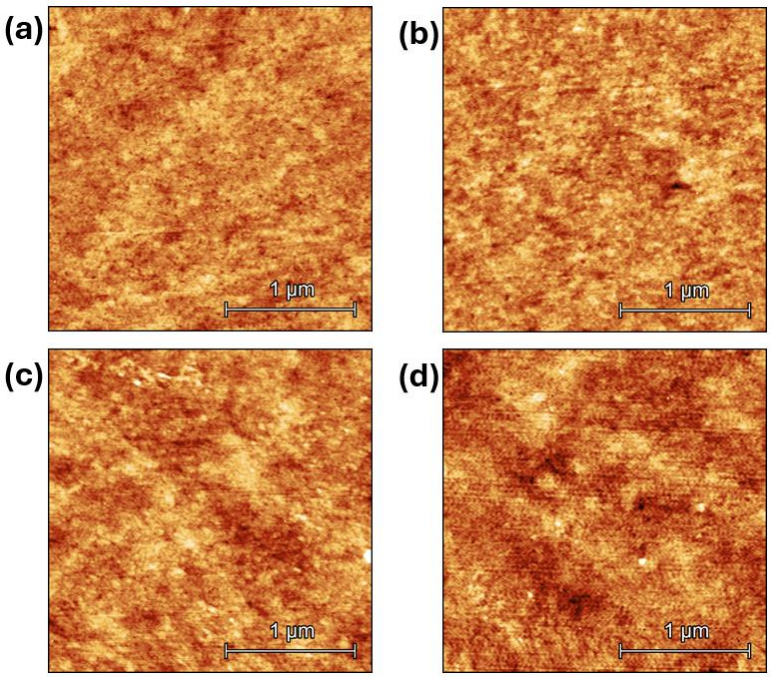

Figure 3.10. (a), (b) Representative AFM images of TSAu substates with RMS roughnesses of 0.26 nm and 0.23 nm. (c) Image of an O1 SAM with RMS roughness of 0.32 nm. (d) Image of an O9 SAM with RMS roughness of 0.30 nm. The scanned area corresponds to 2.5 x 2.5 μm^2 in all images.

XPS spectra of both growth from base-free and basic conditions of O1/O9 SAMs have been analyzed, which include the investigation of Au 4f, C 1s, B 1s, O 1s, and S 2p peaks. Additionally, a TSAu substrate without a monolayer was measured as a reference. As expected, no S 2p or B 1s peaks were observed in the reference sample.

The S 2p peaks are particularly significant as they provide an idea of the number of physisorbed molecules present on the surface. Unbound thiols show slightly higher values of binding energy [77]. The S 2p spectra were fitted by using two doublets. The binding energies for these peaks are given in Table 3.5. In the case of the O1 and O1 basic samples, the first doublets of chemisorbed molecules were recorded at 161.9 eV and 161.7 eV, respectively. The second doublets, corresponding to S-H bonds (unbound thiols), were fitted at 163.4 eV and 163.3 eV, respectively, and showed only minor peaks, as presented in Figure 3.11. Analogously, for the O9 and O9 basic samples, the first doublets were found at 162.2 eV and 162.4 eV, while the second doublets were located at 163.6 eV and 163.7 eV, respectively. These results suggest that a minimal amount of physisorbed molecules are present on the surface, indicating the formation of a well-ordered monolayer. The difference in binding energies between the two doublets is aligned with the previously reported literature values [49], [78]. It was expected for O9 SAMs to exhibit lower $S2p_{3/2}$ binding energies, because sulfur, when bonded with boron, will experience lower withdrawal of electron density compared to bonding with carbon. This is attributed to errors in the XPS equipment and more experiments should be conducted to confirm these results.

The B 1s spectra were fitted using two peaks: one assigned to B-B bonds and the other to B-C bonds. Although other types of boron bonds may exist in the monolayer, their signals in the B 1s spectra are too weak to be meaningful. Therefore, fitting more than two peaks is not practical. The observed peak positions for the B 1s spectra are consistent with values reported in the literature [79].

Fitting for the C 1s spectra involved three peaks for the O1 samples corresponding to a contamination peak, one corresponding to C-B bonds, and one for C-S bonds, while only two were required for the O9 samples; namely a contamination peak and one corresponding to C-B bonds. Surface contamination peaks in C 1s spectra are attributed to environmental exposure of the samples. Similarly, peaks in O 1s were considered surface contamination.

Table 3.5. XPS spectra of O1, O1 basic (O1B), O9, O9 basic (O9B) samples including Au 4f, C 1s, B 1s, O 1s, S 2p peaks. Peak positions (eV), FWHM (eV), and peak areas for each peak are given in the table.

O1	Peak	Peak Position	FWHM	Area	**O1B**	Peak	Peak Position	FWHM	Area
Au4f	$Au4f_{7/2}$	84.0	0.7	223171.0	Au4f	$Au4f_{7/2}$	84.0	0.7	206743.6
	$Au4f_{5/2}$	87.7	0.7	167378.3		$Au4f_{5/2}$	87.7	0.7	155057.7
B1s	$B1s_{1/2}$ (B-B)	188.5	1.9	416.5	B1s	$B1s_{1/2}$ (B-B)	188.4	0.7	135.0
	$B1s_{1/2}$ (B-C)	189.1	2.2	624.8		$B1s_{1/2}$ (B-C)	189.3	0.7	202.5
C1s	$C1s_{1/2}$ (cont.)	284.1	1.6	2937.8	C1s	$C1s_{1/2}$ (cont.)	284.1	1.0	722.0
	$C1s_{1/2}$ (C-B)	284.3	2.2	634.8		$C1s_{1/2}$ (C-B)	284.6	1.7	572.9
	$C1s_{1/2}$ (C-S)	285.7	2.2	634.8		$C1s_{1/2}$ (C-S)	285.0	1.7	572.9
O1s	$O1s_{1/2}$	532.1	1.5	2294.9	O1s	$O1s_{1/2}$	532.4	1.6	1754.2
S2p	$S2p_{3/2}$ (S-Au)	161.9	1.4	1358.3	S2p	$S2p_{3/2}$ (S-Au)	161.7	1.4	1368.6
	$S2p_{1/2}$ (S-Au)	162.9	1.4	679.1		$S2p_{1/2}$ (S-Au)	162.8	1.4	684.3
	$S2p_{3/2}$ (S-H)	163.4	1.4	129.1		$S2p_{3/2}$ (S-H)	163.3	1.4	275.4
	$S2p_{1/2}$ (S-H)	164.5	1.4	64.6		$S2p_{1/2}$ (S-H)	164.4	1.4	137.7
O9	Peak	Peak Position	FWHM	Area	**O9B**	Peak	Peak Position	FWHM	Area
Au4f	$Au4f_{7/2}$	84.0	0.7	200049.8	Au4f	$Au4f_{7/2}$	84.0	0.8	200221.4
	$Au4f_{5/2}$	87.7	0.7	155445.2		$Au4f_{5/2}$	87.7	0.8	150166.0
B1s	$B1s_{1/2}$ (B-B)	188.8	1.7	694.7	B1s	$B1s_{1/2}$ (B-B)	188.6	2.3	825.9
	$B1s_{1/2}$ (B-C)	189.7	1.7	1042.0		$B1s_{1/2}$ (B-C)	189.6	2.3	1238.8
C1s	$C1s_{1/2}$ (cont.)	284.3	1.4	1900.0	C1s	$C1s_{1/2}$ (cont.)	284.0	1.5	1200.0
	$C1s_{1/2}$ (C-B)	285.2	2.2	1264.9		$C1s_{1/2}$ (C-B)	285.1	2.2	1123.1
O1s	$O1s_{1/2}$	532.4	1.9	3322.2	O1s	$O1s_{1/2}$	532.5	2.0	2691.8
S2p	$S2p_{3/2}$ (S-Au)	162.2	1.5	1173.4	S2p	$S2p_{3/2}$ (S-Au)	162.4	1.4	734.9
	$S2p_{1/2}$ (S-Au)	163.3	1.5	586.7		$S2p_{1/2}$ (S-Au)	163.4	1.4	367.5
	$S2p_{3/2}$ (S-H)	163.6	1.5	26.4		$S2p_{3/2}$ (S-H)	163.7	1.4	84.2
	$S2p_{1/2}$ (S-H)	164.7	1.5	13.2		$S2p_{1/2}$ (S-H)	164.7	1.4	42.1

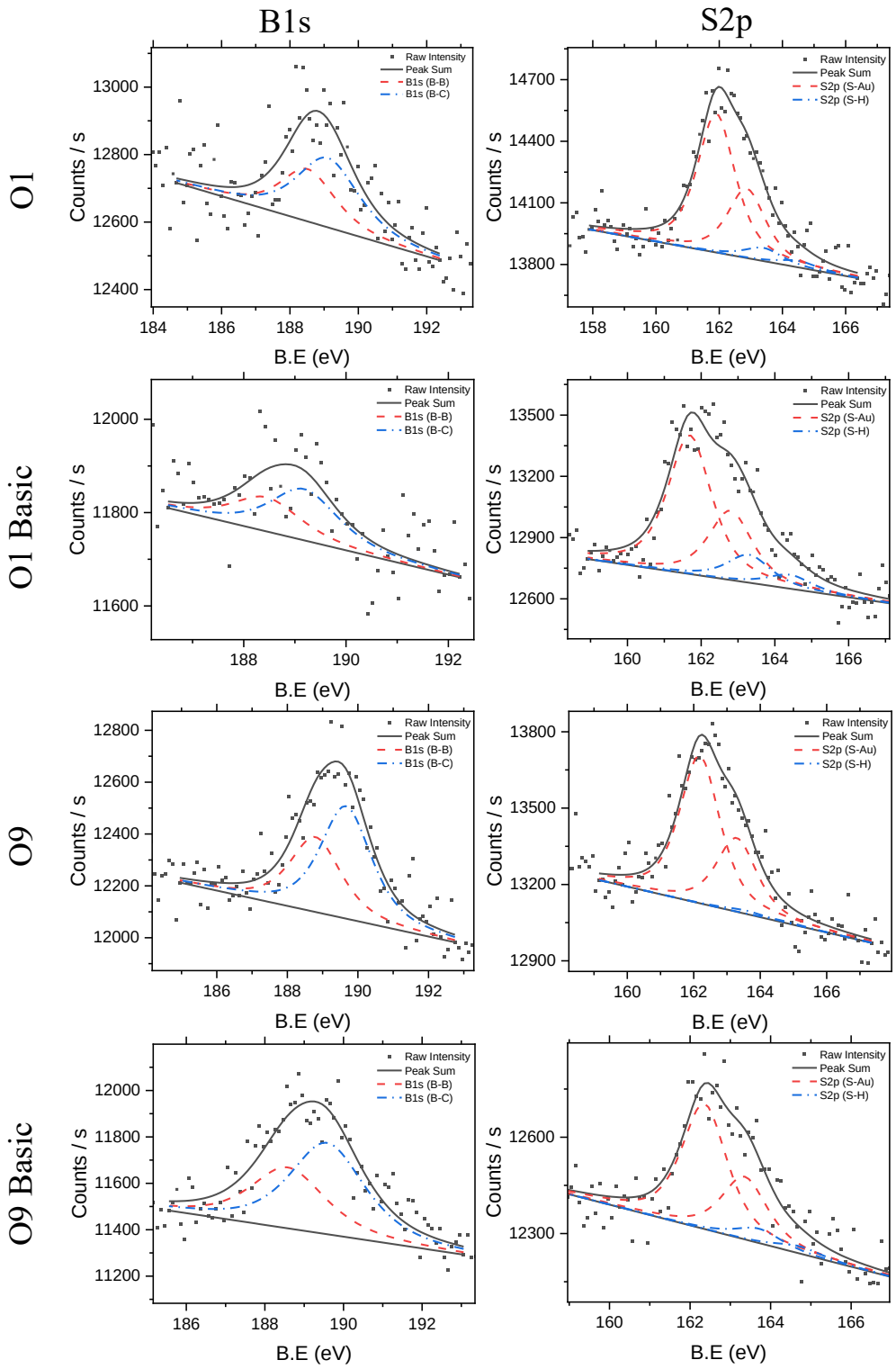

Figure 3.11. XPS spectra of B 1s and S 2p peaks for O1, O1 Basic, O9, and O9 Basic samples.

Based on the analysis of XPS, CA measurements, spectroscopic ellipsometry, and AFM results, it can be concluded that there is no significant difference between the samples prepared in basic conditions or base-free conditions. Both techniques provided SAMs with similar thickness, the same contact angles, and morphological characteristics while also presenting similar surface coverage and chemical composition as observed from XPS spectra. Based on these results, the preparation of SAMs under basic conditions with the addition of NaOH does not have any obvious advantage compared to base-free conditions. For the rest of this thesis, all SAMs were prepared only in base-free conditions without the addition of NaOH. This will avoid unnecessary complications in the preparation step while preserving the integrity and reproducibility of the SAMs.

It was originally planned to do replacement experiments with O1 and O9 SAMs. This involves attempting to replace an existing monolayer with its counterpart derivative by immersing it in the corresponding solution and observing whether the original monolayer would be displaced. However, the experimental results revealed that O1 and O9 exhibit very similar characteristics, including contact angles (CAs), thicknesses, and other physical and chemical properties. The replacement experiments were planned to test whether the H-S-C bond of O1 or the H-S-B bond of O9 would be prepared on the gold surface. Other carboranethiol derivatives will be investigated to explore this phenomenon.

3.3 Bis-carboranethiol SAMs

Unique molecules with two carborane cages and a thiol group, mm-SH and pp-SH, were characterized in this part of the thesis. They both bond to the surface with the H-S-C bond, so they are not compatible to test the H-S-B bond, however, there is no previous work investigating these isomers in the literature. Comparing these two isomers helps us understand the behavior of different bonding and chemical states.

3.3.1 Pristine mmSH and ppSH SAMs

Similar CA results were initially expected with mm-SH and pp-SH due to their similar chemical structures; however, their CAs differ significantly. In Figure 3.12, the average CAs of nine samples of both mm-SH and pp-SH SAMs on Au(111) surfaces were presented. Hysteresis values for pp-SH are much lower compared to mm-SH, indicating chemically smoother and more ordered surfaces. The lower standard deviation in the CAs of pp-SH samples further supports this interpretation. In general, the standard deviation in the CAs of these SAMs is considerably lower compared to O1 and O9 SAMs. These observations may be related to the 3D structure of bis-carboranethiols effectively filling the vacancy islands, producing a more homogeneous surface; however, further experiments are necessary to confirm this

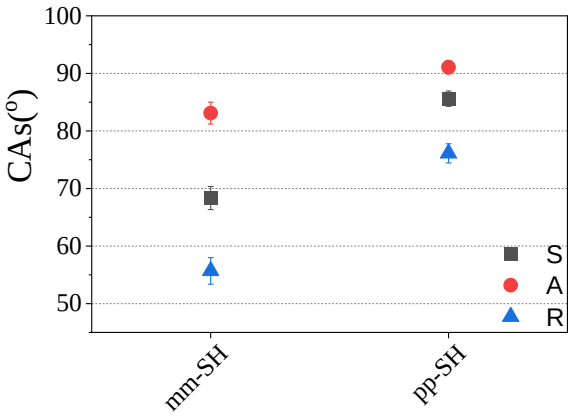

Figure 3.12. CA averages of 9 mm-SH and 9 pp-SH samples.

Table 3.6. The numerical values of the data points shown in Figure 3.12.

	S	A	R	Δ
mm-SH	68.3 ± 2.0	83.1 ± 1.9	55.7 ± 2.3	27.4
pp-SH	85.6 ± 1.3	91.1 ± 1.2	76.1 ± 1.7	15.0

In Figure 3.13, CA results obtained with different test liquids are shown. Four samples were measured with glycerol (GC), ethylene glycol (EG), and dimethyl

sulfoxide (DMSO) for each type of SAM. Additionally, the deionized (DI) water results of nine samples were included in the graph. These results reveal trends between mm-SH and pp-SH. Although the CA values for these two molecules are very similar (with CAs for pp-SH consistently higher), hysteresis values for mm-SH are greater. Receding measurements for mm-SH could not be obtained with EG, unlike for pp-SH. The primary causes of CA hysteresis are surface roughness and chemical inhomogeneities. Thus, these results suggest that pp-SH molecules exhibit better ordering on the surface.

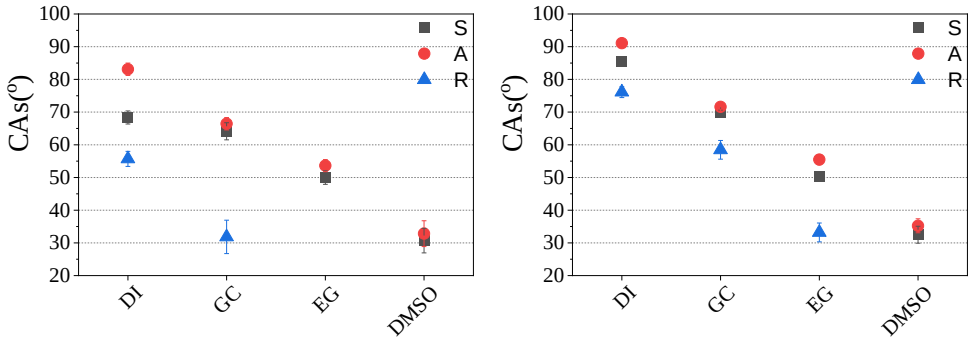

Figure 3.13. Contact angles of mm-SH (left) and pp-SH (right) were measured with four different types of liquids.

Table 3.7. The numerical values of the data points shown in Figure 3.13.

		S	A	R	Δ
mm-SH	DI	68.3 ± 2.0	83.1 ± 1.9	55.7 ± 2.3	27.4
	GC	64.1 ± 2.6	66.4 ± 1.9	31.8 ± 5.1	34.6
	EG	50.0 ± 2.1	53.6 ± 1.9		
	DMSO	30.7 ± 3.8	32.8 ± 3.9		
pp-SH	DI	85.6 ± 1.3	91.1 ± 1.2	76.1 ± 1.7	15.0
	GC	69.9 ± 0.8	71.6 ± 0.7	58.5 ± 2.9	13.1
	EG	50.4 ± 1.3	55.5 ± 1.6	33.2 ± 2.9	22.3
	DMSO	32.5 ± 2.6	35.2 ± 2.1		

Testing surfaces with various liquids is particularly important for surface energetics calculations. These liquids provide a range of intermolecular forces, enabling a deeper understanding of solid-liquid and solid-vapor interactions. The CA results obtained with these test liquids and mm-SH and pp-SH molecules can be used to calculate the solid surface energy and analyze the structural differences between the two types of carboranethiol SAMs. Equation of state (EoS) approach with modified Berthelot's rule, explained in Chapter 2, were used to calculate solid surface tensions of mm-SH and pp-SH SAMs. Advancing CAs were used to calculate $cos\theta_Y$ since low-rate advancing CAs are considered to be best approximations of Young's contact angle [53]. Experimental values of $cos\theta_Y$ and liquid surface tensions, γ_{lv}, of test liquids are shown in Figure 3.14. Curves represent best fits of Eq. 8, yielding calculated solid surface tensions of 35.1 mJ/m² for mm-SH and 34.9 mJ/m² for pp-SH SAMs. β value of mm-SH is 0.0001394 $(m^2/mJ)^2$, which is very close to the literature average of 0.0001247 $(m^2/mJ)^2$ [67]. In contrast, the β value of pp-SH surfaces are 0.0002221. This deviation might suggest unique interactions, possibly due to structural differences. While the CA measurements using DI water show a significant difference between mm-SH and pp-SH SAMs, their solid surface tensions remain comparable. This finding implies similar intermolecular forces between the two surfaces despite their structural differences.

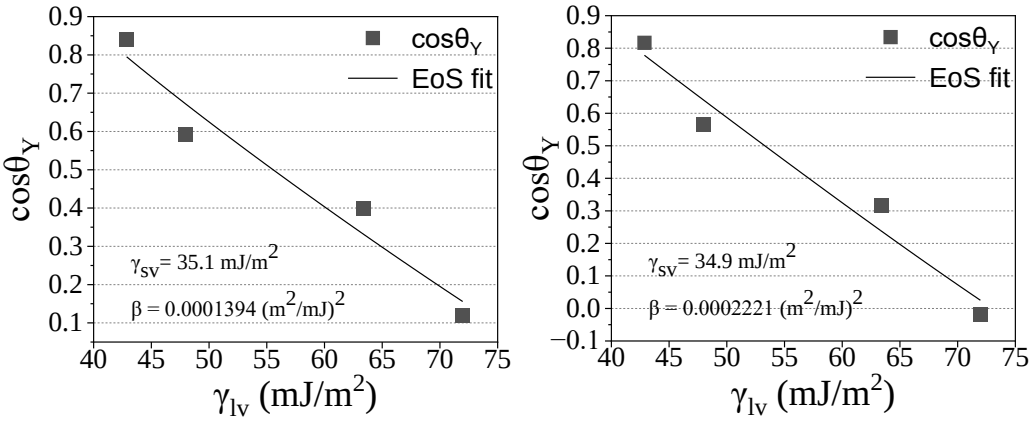

Figure 3.14. $cos\theta_Y$ vs. γ_{lv} for mm-SH (left) and pp-SH (right) surfaces. The curves are best-fits of Eq. 8 to experimental data points. Obtained values of γ_{sv} for mm-SH is 35.1 mJ/m^2, for pp-SH is 34.9 mJ/m^2.

Ellipsometric measurements of mm-SH and pp-SH SAMs were conducted to determine monolayer thickness. Thickness values of six samples for each type of SAM were averaged. From Figure 3.15, it can be seen that both mm-SH and pp-SH samples have an average thickness of about 0.82 nm. However, the standard deviation of mm-SH is significantly higher indicating a larger variation of the film thickness between samples. The variation of mm-SH indicates that mm-SH molecules form less homogeneous monolayers on the gold surface compared to pp-SH molecules. The higher stability of pp-SH molecules on the gold surface may be caused by the differences in molecular structure, packing density, or strength of thiol-gold bonds. Such structural differences likely result in better molecular ordering and fewer defects or surface irregularities in pp-SH monolayers. The lower CA hysteresis and reduced variability in the thickness measurement of pp-SH further imply better structural stability and thus a more reliable candidate for applications requiring uniform surface properties.

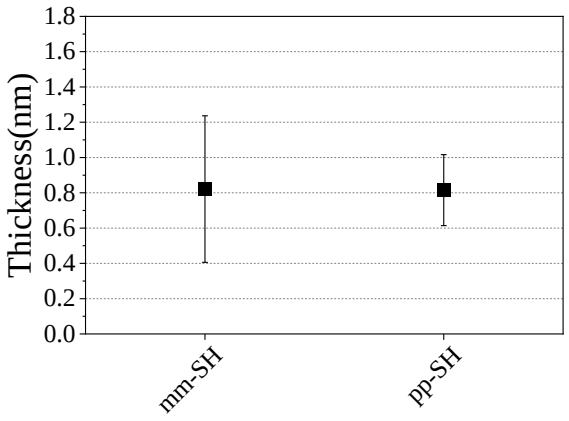

Figure 3.15. Average thickness values of mm-SH and pp-SH samples obtained with spectroscopic ellipsometry.

AFM analysis of mm-SH and pp-SH samples gave average roughness values in the range of 0.25 nm to 0.55 nm. Representative topographical images of the monolayer surfaces are presented in Figure 3.16. Grain boundaries and pinholes can be observed on the surface; however, these defects are due to the TSAu substrates used when working with mm-SH and pp-SH. The deposition of the monolayer does not significantly influence the topography of the surface. However, AFM characterization was necessary to detect the aggregations on the surface that could considerably affect the values of CAs or thickness obtained by spectroscopic ellipsometry. The increased roughness of mm-SH samples in comparison to pp-SH samples is another point that confirms the more ordered and defect-free packing of pp-SH into monolayers. All these findings agree with contact angle and ellipsometry data and lead to the same conclusion regarding better packing and stability of pp-SH monolayers.

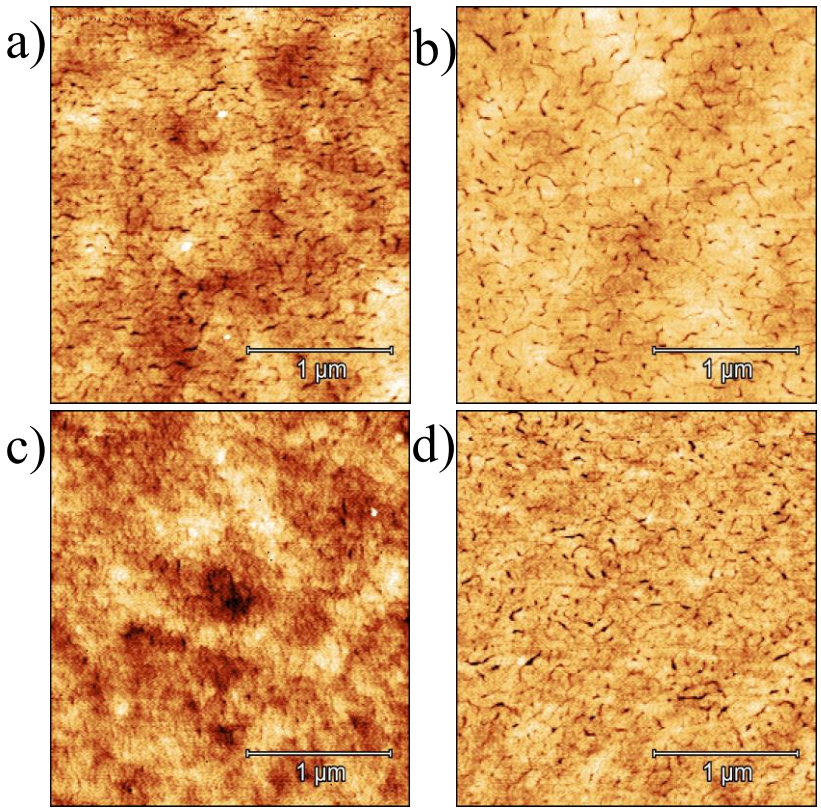

Figure 3.16. (a), (b) Representative AFM images of mm-SH samples with RMS roughnesses of 0.41 nm and 0.55 nm. (c), (d) Representative AFM images of pp-SH samples with RMS roughnesses of 0.28 nm and 0.42 nm.

3.3.2 mm-SH and pp-SH stability and replacement experiments

To test the stability of the monolayers, samples were kept in ethanol for 5 days. CA was measured each day for 5 days. The results can be seen in Figures 3.17 and 3.18. In five days, the pp-SH SAMs showed lower hysteresis values and less pronounced decreases in CAs, which is indicative of higher structural stability and greater resistance of the thiolate layer to the progress of the solvent-induced degradation process. In contrast, mm-SH monolayers show a more pronounced drop in CA and higher hysteresis values, indicative of weaker molecular packing and high susceptibility to structural disruption. These results are in good agreement with the better molecular ordering speculated for pp-SH monolayers by CA measurements

and ellipsometry. Higher packing density, stronger thiol-gold bonds, and more homogeneous surface coverage could be the reasons for the stability of pp-SH monolayers. Further stability experiments beyond five days could give more information about the long-term performance and degradation processes of such monolayers.

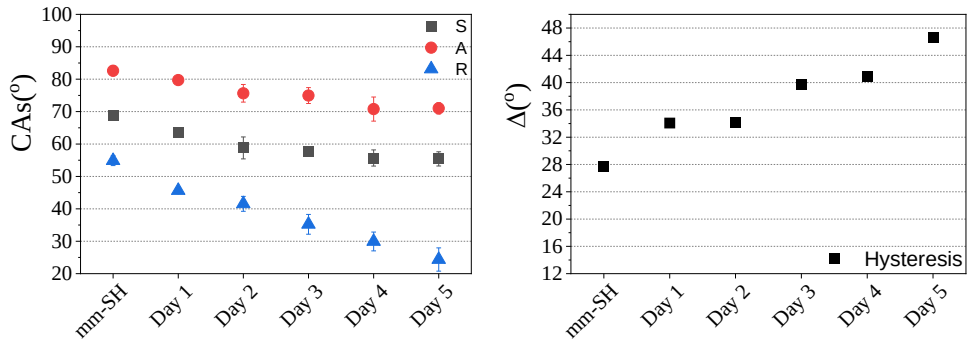

Figure 3.17. An mm-SH sample was immersed in ethanol for 5 days to test its stability in the solvent. Hysteresis values were added in a separate graph.

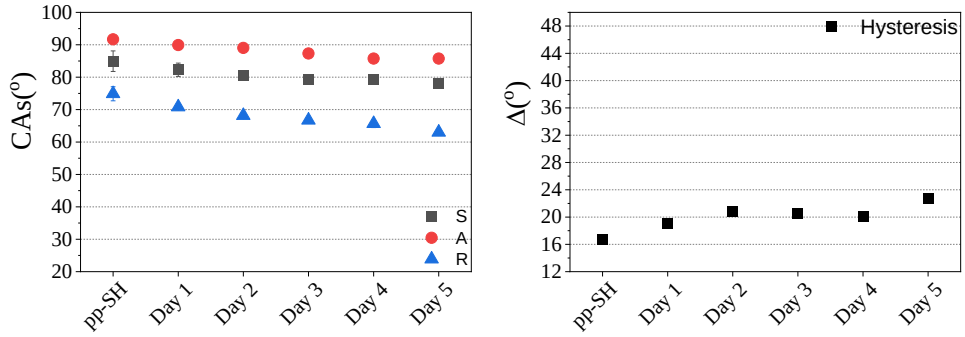

Figure 3.18. A pp-SH sample was immersed in ethanol for 5 days to test its stability in the solvent. Hysteresis values were added in a separate graph.

To understand the nature of those molecules on gold surfaces, replacement experiments were conducted. A mm-SH sample was immersed in a pp-SH solution for 5 days, and vice versa. Samples were taken out of their solutions each day for contact angle measurements. Contact angles were also measured before the immersion to the replacement solution.

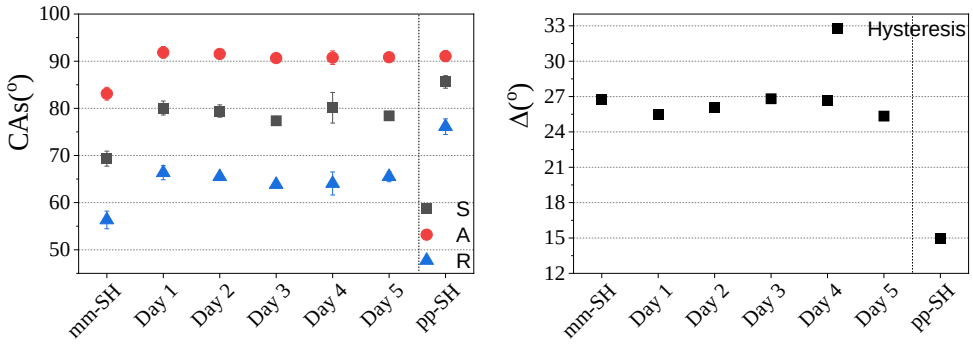

Figure 3.19. Replacement of mm-SH molecules with pp-SH molecules on TSAu surface. mm-SH molecules were kept inside the pp-SH solution for 5 days. CA was recorded each day. The average of all pp-SH measurements was also added to the right side of the graph for comparison. Hysteresis values were added in a separate graph.

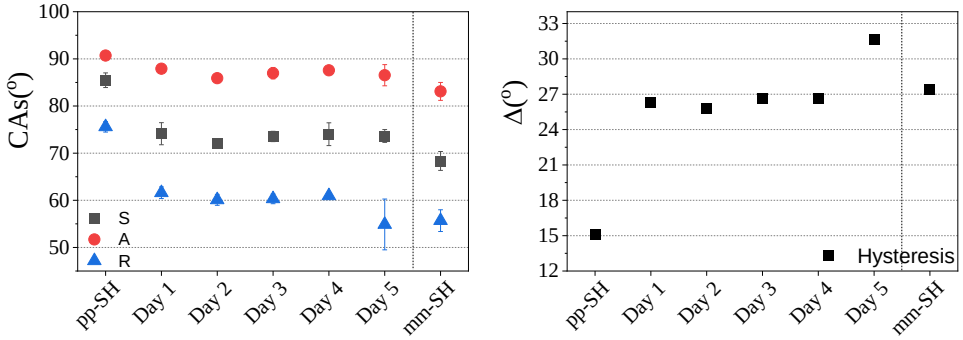

Figure 3.20. Replacement of pp-SH molecules with mm-SH molecules on TSAu surface. pp-SH molecules were kept inside mm-SH solution for 5 days. CA was recorded each day. The average of all mm-SH measurements was also added to the right side of the graph for comparison. Hysteresis values were added in a separate graph.

As can be seen from the data, neither molecule fully replaces the other within the five-day period. When mm-SH samples were immersed in a pp-SH solution, the hysteresis value remained largely constant, with only a slight decrease over five days, suggesting minimal molecular displacement. However, the advancing contact angle of mm-SH increased largely on the first day, reaching values similar to pp-SH. This dynamic would seem to reflect the adsorption of pp-SH molecules onto the pre-

existing mm-SH layer, changing the wetting properties without displacing the monolayer. The stable hysteresis suggests that though there are some molecular interactions, the mm-SH SAM stays mainly intact. In the case of the pp-SH samples immersed in the mm-SH solution, hysteresis increased rapidly to values comparable to that for mm-SH within even the first day, suggesting disruption of the original pp-SH monolayer. The advancing contact angle for pp-SH was found to decrease progressively over the five-day period, showing a gradual decrease in hydrophobicity and adsorption of mm-SH molecules. Generally, the results of replacement experiments suggest complex molecular interactions between mm-SH and pp-SH on the gold surface; however, the observed changes in the contact angles and hysteresis values indicate that neither molecule fully replaces the other under the given conditions.

3.4 diME-O9 and P1C replacement experiments

To test the hypothesis regarding which type of bonds are preferred on the surface (H-S-C or H-S-B), CA measurements with two new carboranethiol derivatives, diME-O9 and P1C, were employed. diME-O9 was expected to form hydrophobic monolayers, whereas P1C was anticipated to yield a hydrophilic surface. P1C is bonded to the surface via Au-S-C bonds, which were hypothesized to be preferred over the Au-S-B bonds of diME-O9 samples. Their SAMs on silver substrates were also analyzed since they are less inert compared to gold, to determine if there are differences in binding characteristics. The silver surfaces were prepared using the template-stripping method, similar to the gold surfaces. However, template stripping results in polycrystalline silver surfaces [80], so careful interpretation of the data is necessary, as CA measurements are sensitive to surface roughness and chemical homogeneity. AFM images of the silver and gold surfaces used are presented in Figure 3.21.

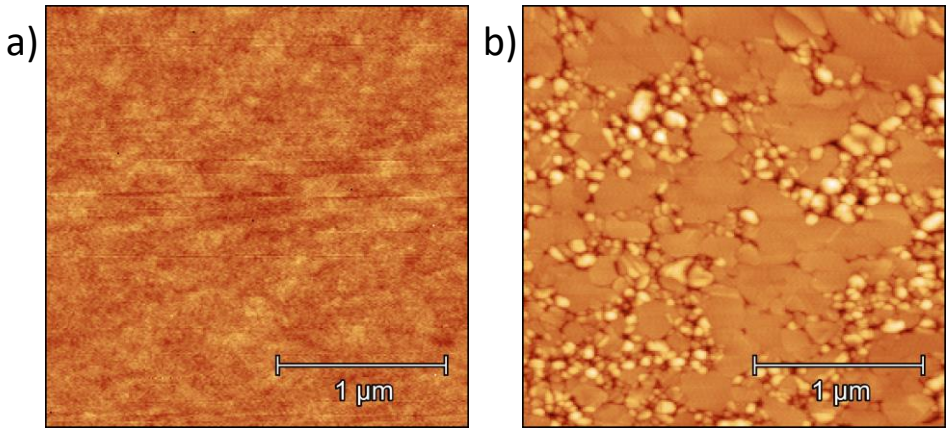

Figure 3.21. AFM images of (a) Template-stripped gold surface with RMS roughness of 0.18 nm, (b) Template-stripped silver surface with RMS roughness of 1.55 nm.

Figures 3.22 and 3.23 show the results of replacement experiments. Each sample was immersed in its opposing solution, and the CAs of the samples were measured for 5 days and on day 14. Two samples were measured for each experiment. The stability of P1C SAMs was found to be very high for gold surfaces. The CA values for P1C SAMs did not change over the 14-day period, apart from the first day, indicating a highly stable monolayer. The decrease on the first day could be attributed to the reordering of the P1C structure. In contrast, the CAs of diME-O9 SAMs gradually decreased, approaching the values of P1C SAMs, particularly after two weeks. That implies a gradual replacement or reorganization of the diME-O9 monolayer and thus supports the hypothesis that Au-S-C bonds of P1C SAMs are thermodynamically more favorable compared with Au-S-B bonds of diME-O9 SAMs and explains why P1C would dominate after some time. However, such a finding needs more experimental confirmation.

For Ag substrates, the CA values converged for both SAMs to an intermediate level. This implies a lack of selectivity and stability in bonding, likely due to the weaker binding interactions on silver surfaces. Furthermore, the higher RMS roughness of the silver surfaces (1.55 nm) compared with that of gold surfaces (0.18 nm) enhances this effect, since increased roughness destabilizes monolayer organization and

enhances contact angle variability. The weaker, less stable bonding on silver surfaces is responsible for significant rearrangement or mixing of the SAMs regardless of their original composition

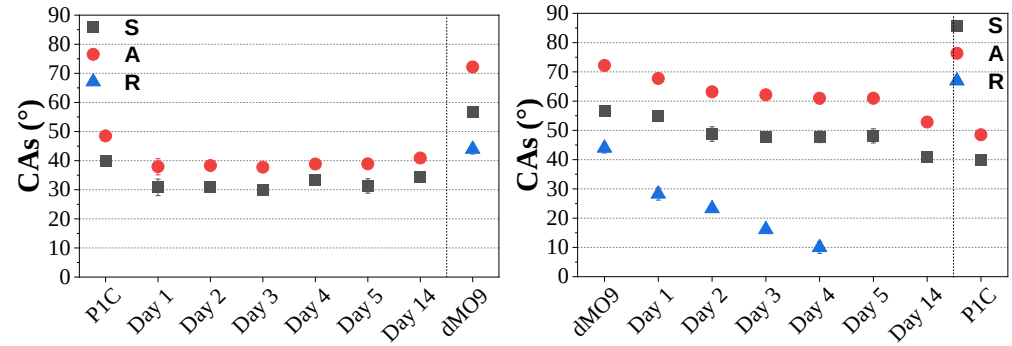

.

Figure 3.22. Replacement experiments on TSAu surfaces. 2 P1C samples were immersed in diMe-O9 solution and vice versa. CA of samples was measured for 5 days and at day 14. For comparison, the average CA values of the opposing samples were included on the right side of graphs.

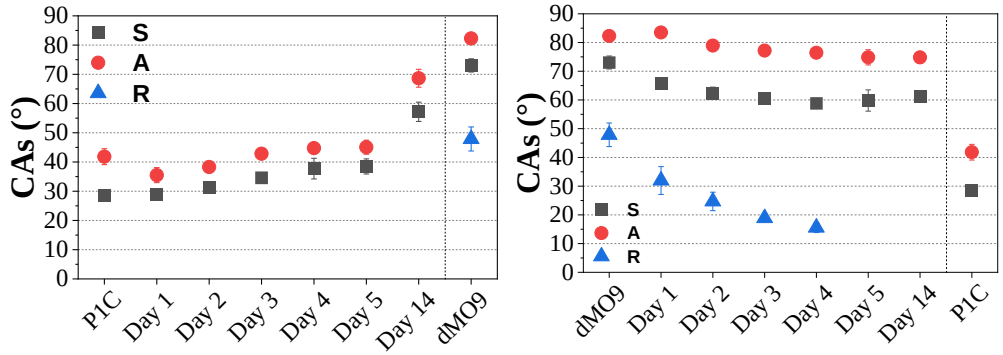

Figure 3.23. Replacement experiments on TSAg surfaces. 2 P1C samples were immersed in diMe-O9 solution and vice versa. CA of samples was measured for 5 days and at day 14. For comparison, the average CA values of the opposing samples were included on the right side of the graphs.

3.5 Vacuum growth with SMBD

This section describes the growth and characterization of ODT and O9 SAMs under vacuum conditions, using the SMBD technique. Because of the experimental complications, their characterization was restricted to the assessment of the presence and ordering of the monolayer. This limitation is due to the scarcity of data regarding thiol-based monolayers prepared under vacuum conditions. More precisely, the optimal conditions, such as the appropriate kinetic energies for these molecules, especially for O9, are not known. Additionally, it should be noted that the growth rate of these molecules cannot be measured due to the noise present in the QCM instrument. The source of the noise might be environmental vibrations such as vacuum pumps, or thermal instabilities that decreased the signal-to-noise ratio to values too low to resolve the incremental mass changes due to monolayer formation.

3.5.1 ODT growth in vacuum

As explained in Chapter 2, all of the samples were washed with ethanol before characterization; however, in the case of the SAMs grown in vacuum, there was a significant difference between the contact angles of washed versus unwashed samples. It indicates that physisorbed molecules tend to build up onto the surface of the SAM, showing that the washing step is indeed important for removing loosely bound species. CAs of an ODT sample grown using SMBD before and after washing can be seen in Figure 3.24.

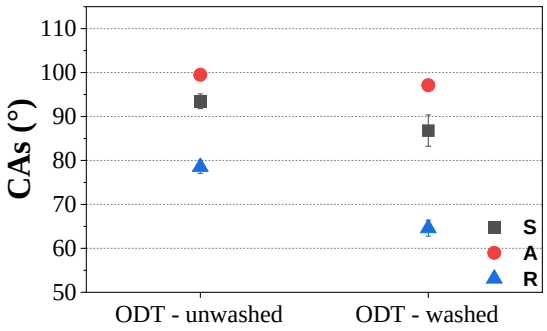

Figure 3.24. CAs of an ODT SAM grown using SMBD. The graph shows the CA of the same sample before and after washing.

The CAs of ODT SAMs grown under various conditions are shown in Figure 3.25. All samples were washed as previously described. The CA of a TSAu substrate is also presented. This substrate was kept in a vacuum chamber, similar to the other samples coated with ODT. Additionally, an ODT SAM grown from a solution is included on the right side of the graph. Unlike the other samples, the ODT–4 SAM was grown on a TSAg substrate (TSAu is the main substrate of choice unless specified otherwise). The growth conditions are detailed in Table 3.8. Based on prior experiments, 140 °C was determined to be the optimal temperature for ODT molecules. This temperature was measured using a thermocouple placed at the side of the heating element. All samples were grown under these conditions.

Table 3.8. Source chamber temperature and growth times of ODT SAMs shown in Figure 3.25.

Sample	ODT – 1	ODT – 2	ODT – 3	ODT – 4 (Ag)
Temperature (°C)	139.6	139.5	139.8	139.8
Growth Time (min)	20	30	60	30

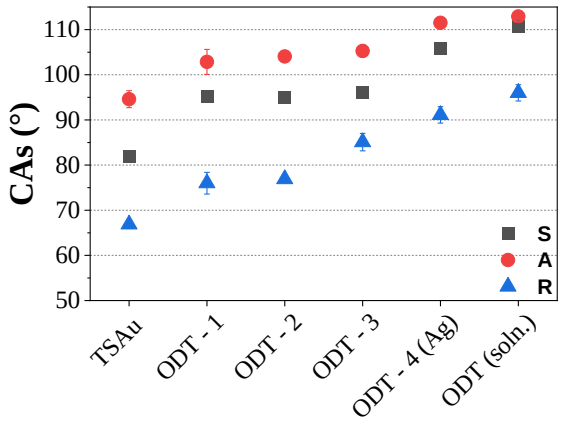

Figure 3.25. CAs of ODT SAMs grown under various conditions. The CA of the TSAu substrate is included as a reference. ODT samples 1–4 were grown under vacuum conditions, with growth times of 20, 30, 60, and 30 minutes, respectively. ODT-4 was grown on a TSAg substrate. The average CAs of ODT SAMs grown from the solution are shown on the right for comparison.

It was observed that growth time affects the CAs of ODT samples, as it gets closer to the CA of samples grown from solution. Also, due to its less inert nature, SAM grown on top of TSAg shows higher CA, closer to the SAM grown from solution. This trend suggests that extended growth times allow for a more complete and uniform monolayer formation, leading to properties that more closely resemble those of solution-grown SAMs. The higher CA observed for the SAM on TSAg may be attributed to the enhanced interactions between the thiol molecules and the less inert silver surface, which promotes better molecular alignment and packing. However, CA goniometry is a highly speculative method for evaluating monolayer quality, and further characterization is necessary to understand why ODT SAMs grown under vacuum conditions do not achieve properties identical to those grown in solution. Key kinetic differences between solution and vacuum growth methods explained in Chapter 1 likely contribute to this disparity. In solution-phase growth, thiol molecules diffuse freely in a liquid medium, enabling rapid adsorption, dynamic rearrangement, and displacement of weakly bound molecules. In vacuum, molecules attach slowly and can’t rearrange as easily, which might lead to looser, less orderly layers, even with extra time.

3.5.2 O9 growth in vacuum

The contact angles (CAs) of O9 self-assembled monolayers (SAMs) grown under vacuum conditions were analyzed to assess the effects of growth parameters and substrate properties. Figure 3.26 displays the CAs of vacuum-grown samples (O9-1, O9-2, O9-3, and O9-4), with the final data point representing O9 SAMs grown from solution. CA values of TSAu substrate kept in vacuum environment were also added for reference. As summarized in Table 3.9, the vacuum-grown samples were prepared at progressively higher temperatures and varying growth times, ranging from 10 to 30 minutes. The results indicate that higher growth temperatures and longer deposition times lead to little to no change in CAs, reflecting higher temperatures are not needed for the growth of O9. The sample O9-4 was grown on top of the TSAg substrate, but the CA of the sample is still comparable with the other samples.

Table 3.9. Source chamber temperature and growth times of ODT SAMs shown in Figure 3.26.

Sample	O9 – 1	O9 – 2	O9 – 3	O9 – 4 (Ag)
Temperature (°C)	63.1	78.9	117.2	78.8
Growth Time (min)	10	20	30	20

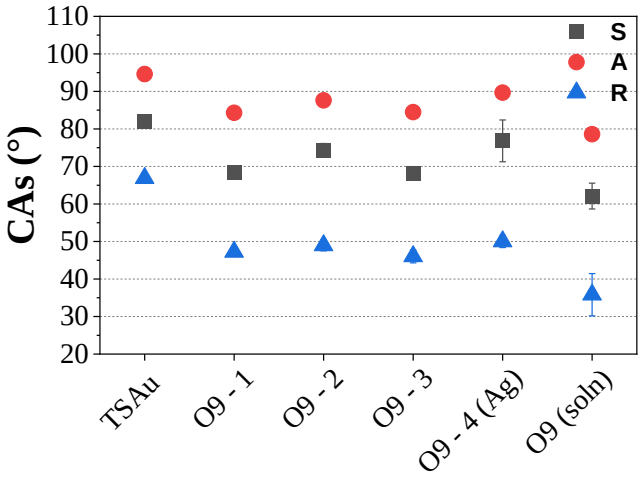

Figure 3.26. CAs of O9 SAMs grown under various conditions. The CA of the TSAu substrate is included as a reference. O9 samples 1–4 were grown under vacuum conditions, with growth times of 10, 20, 30, and 20 minutes, respectively. O9-4 was grown on a TSAg substrate. The average CAs of O9 SAMs grown from the solution are shown on the right for comparison.

The role of physisorbed molecules also affects the CA results. Vacuum-grown samples are more susceptible to physisorption due to the absence of a solvent medium, which helps remove loosely bound species during solution-based growth. This surface heterogeneity caused by physisorbed molecules can change the apparent CA values. To examine stability, replacement experiments were conducted for the vacuum-grown monolayers. Accordingly, O9 samples (O9–1 and O9–3) were immersed in the P1C solution to see whether the monolayers would be replaced by the P1C layers. The samples remained in the P1C solution for three days, and the results are presented in Figure 3.27. For comparison, the CA of a P1C monolayer grown from solution, obtained via a one-day solution growth, was also included in the graph. As can be seen, P1C could not completely replace the O9 SAMs grown using the SMBD technique. By comparing the replacement experiments of diMe-O9 and P1C of Chapter 3.4, it can be further inferred that O9 monolayers are significantly more stable than solution-grown diMe-O9 monolayers. Again, considering the limitations in making a direct comparison between different

molecules, results suggest that the O9 monolayers are inherently more stable under these experimental conditions. Additional work will be required to confirm the observations.

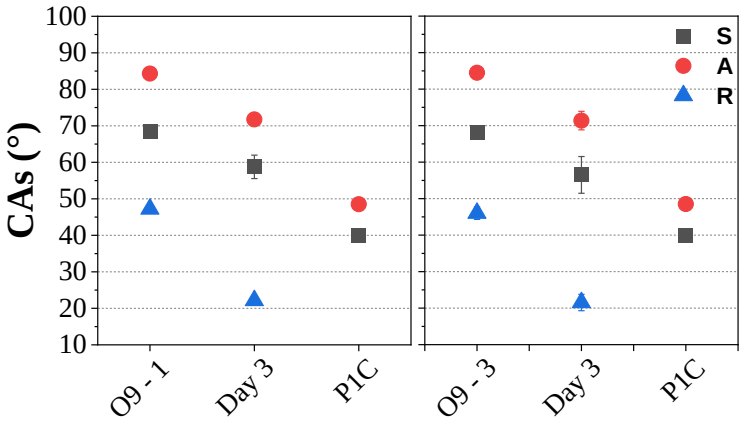

Figure 3.27. Replacement experiments of O9 samples grown in a vacuum. The samples were immersed in P1C solution for three days. The CA of a P1C monolayer grown from solution was added for reference.

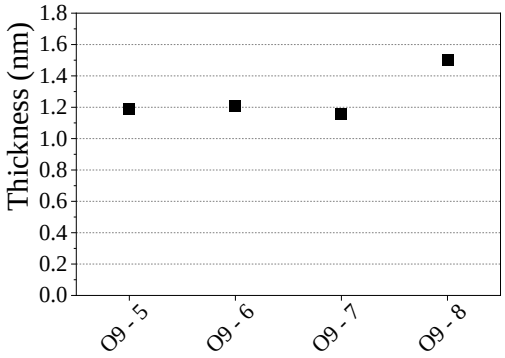

Figure 3.28. Thickness values of O9 samples grown in a vacuum, obtained using spectroscopic ellipsometry.

Spectroscopic ellipsometry SAM thickness results of O9 SAMs grown in vacuum can be seen in Figure 3.28. To distinguish them from the previously analyzed samples, the samples are labeled 5 through 8. All the samples in this figure were grown at a constant temperature of 63°C. There was no need to grow the samples at higher temperatures since there was no significant difference in CAs. For the samples 5, 6, 7, and 8, the growth time was chosen as 10, 15, 20, and 25 minutes, correspondingly. The measured thickness is very much larger compared to the maximum molecular thickness of 0.85 nm. These results can indicate the complex growth procedure and presence of physisorbed molecules in line with chemisorbed molecules.

CHAPTER 4

CONCLUSION

The study focused on the relations between the molecular structure, bonding, and surface properties of SAMs. Experimental work and analysis were carried out to understand the behavior under different conditions of carboranethiol self-assembled monolayers on gold and silver substrates. The most important conclusion is that there were no significant differences in thickness, contact angles, or morphology for SAMs prepared under base-free and basic conditions. This is in very good agreement with data from XPS, contact angle (CA) measurements, and spectroscopic ellipsometry. The preparation of SAMs under base-free conditions simplifies the process and ensures consistency. The study also compared O1 and O9 SAMs, finding properties between the two that were very similar despite minor differences. The research on the bis-carboranethiol SAMs has pointed out the differences among the mm-SH and pp-SH isomers. Indeed, the pp-SH forms more ordered and stable monolayers with fewer defects than those of mm-SH. Indeed, pp-SH was composed of smoother surfaces and presented fewer irregularities, which AFM imaging has confirmed. This would surely make pp-SH an overall better option when stable and uniform surfaces are in demand. Stability and replacement tests provide additional information. The pp-SH monolayers were more stable in ethanol than the less consistent mm-SH complex. It also investigated diME-O9 and P1C SAMs with special emphasis on bonding preferences and properties of the surface. In fact, P1C with its Au-S-C bonds gave stable, hydrophilic monolayers on gold, whereas the one with Au-S-B bonds-exposing diME-O9 was less stable. Replacement experiments gave evidence of P1C gradually replacing diME-O9 and hence a thermodynamic preference for Au-S-C bonds. On silver, on the other hand, the two SAMs exhibited less stability and selectivity due to weaker bonding and rough surface. Vacuum growth using SMBD for ODT and O9 SAMs highlighted challenges, including

physisorption effects, limited characterization data, and experimental constraints like noise in QCM measurements. For ODT, longer deposition times improved uniformity, but vacuum-grown SAMs remained distinct from solution-grown ones. For O9, growth temperature had minimal impact on contact angles, and the monolayers demonstrated inherent stability under experimental conditions, outperforming solution-grown diMe-O9. Replacement experiments showed that O9 SAMs were not fully replaced by P1C, demonstrating higher stability.

This work provides an overview of the structure, bonding, and stability of carboranethiol SAMs, which will add to designing SAMs for desired applications. Further studies can be focused on other derivatives, and advanced analysis techniques could also be employed; further extension of stability tests will explain the behavior of SAMs in applications in nanotechnology and material science.

REFERENCES

[1] F. Schreiber, “Structure and growth of self-assembling monolayers,” *Prog Surf Sci*, vol. 65, no. 5–8, pp. 151–257, Nov. 2000, doi: 10.1016/S0079-6816(00)00024-1.

[2] I. Langmuir, “The constitution and fundamental properties of solids and liquids. II. Liquids,” *J Am Chem Soc*, vol. 39, no. 9, pp. 1848–1906, Sep. 1917, doi: 10.1021/JA02254A006/ASSET/JA02254A006.FP.PNG_V03.

[3] I. Langmuir, “The mechanism of the surface phenomena of flotation,” *Transactions of the Faraday Society*, vol. 15, no. June, pp. 62–74, Jan. 1920, doi: 10.1039/TF9201500062.

[4] K. B. Blodgett, “Films Built by Depositing Successive Monomolecular Layers on a Solid Surface,” *J Am Chem Soc*, vol. 57, no. 6, pp. 1007–1022, Jun. 1935, doi: 10.1021/JA01309A011/ASSET/JA01309A011.FP.PNG_V03.

[5] K. B. Blodgett and I. Langmuir, “Built-Up Films of Barium Stearate and Their Optical Properties,” *Physical Review*, vol. 51, no. 11, p. 964, Jun. 1937, doi: 10.1103/PhysRev.51.964.

[6] G. M. Whitesides and B. Grzybowski, “Self-Assembly at All Scales,” *Science (1979)*, vol. 295, no. 5564, pp. 2418–2421, Mar. 2002, doi: 10.1126/SCIENCE.1070821.

[7] J. C. Love, L. A. Estroff, J. K. Kriebel, R. G. Nuzzo, and G. M. Whitesides, “Self-assembled monolayers of thiolates on metals as a form of nanotechnology,” *Chem Rev*, vol. 105, no. 4, pp. 1103–1169, Apr. 2005, doi: 10.1021/CR0300789.

[8] S. Zhang, “Fabrication of novel biomaterials through molecular self-assembly,” *Nature Biotechnology 2003 21:10*, vol. 21, no. 10, pp. 1171–1178, Sep. 2003, doi: 10.1038/nbt874.

[9] C. Vericat, M. E. Vela, G. Benitez, P. Carro, and R. C. Salvarezza, “Self-assembled monolayers of thiols and dithiols on gold: new challenges for a well-known system,” 2010, doi: 10.1039/b907301a.

[10] P. E. Laibinis, G. M. Whitesides, D. L. Aliara, Y. T. Tao, A. N. Parikh, and R. G. Nuzzo, “Comparison of the Structures and Wetting Properties of Self-Assembled Monolayers of n-Alkanethiols on the Coinage Metal Surfaces, Cu, Ag, Au,” *J Am Chem Soc*, vol. 113, no. 19, pp. 7152–7167, Sep. 1991, doi: 10.1021/JA00019A011/SUPPL_FILE/JA00019A011_SI_001.PDF.

[11] G. M. Whitesides, J. K. Kriebel, and J. C. Love, “Molecular engineering of Surfaces Using Self-Assembled Monolayers,” *https://doi.org/10.3184/003685005783238462*, vol. 88, no. Pt 1, pp. 17–48, Feb. 2005, doi: 10.3184/003685005783238462.

[12] D. Wang and H. Dai, “Germanium nanowires: From synthesis, surface chemistry, and assembly to devices,” *Appl Phys A Mater Sci Process*, vol. 85, no. 3, pp. 217–225, Nov. 2006, doi: 10.1007/S00339-006-3704-Z/METRICS.

[13] N. Muskal and D. Mandler, “Thiol self-assembled monolayers on mercury surfaces: the adsorption and electrochemistry of ω-mercaptoalkanoic acids,” *Electrochim Acta*, vol. 45, no. 4–5, pp. 537–548, Nov. 1999, doi: 10.1016/S0013-4686(99)00232-7.

[14] Z. Mekhalif, F. Laffineur, N. Couturier, and J. Delhalle, “Elaboration of Self-Assembled Monolayers of n-Alkanethiols on Nickel Polycrystalline Substrates: Time, Concentration, and Solvent Effects,” *Langmuir*, vol. 19, no. 3, pp. 637–645, 2003, Accessed: Sep. 12,

2024. [Online]. Available: https://researchportal.unamur.be/en/publications/elaboration-of-self-assembled-monolayers-of-n-alkanethiols-on-nic

[15] C. K. Yee *et al.*, “Novel One-Phase Synthesis of Thiol-Functionalized Gold, Palladium, and Iridium Nanoparticles Using Superhydride,” 1999, doi: 10.1021/la990015e.

[16] F. Sinapi, L. Forget, J. Delhalle, and Z. Mekhalif, “Self-assembly of (3-mercaptopropyl)trimethoxysilane on polycrystalline zinc substrates towards corrosion protection,” *Appl Surf Sci*, vol. 212–213, no. SPEC., pp. 464–471, May 2003, doi: 10.1016/S0169-4332(03)00142-9.

[17] O. Voznyy and J. J. Dubowski, “Structure of thiol self-assembled monolayers commensurate with the GaAs (001) surface,” *Langmuir*, vol. 24, no. 23, pp. 13299–13305, Dec. 2008, doi: 10.1021/LA8010635/SUPPL_FILE/LA8010635_SI_008.XYZ.

[18] A. C. Mendes, E. T. Baran, R. L. Reis, and H. S. Azevedo, “Self-assembly in nature: using the principles of nature to create complex nanobiomaterials,” *Wiley Interdiscip Rev Nanomed Nanobiotechnol*, vol. 5, no. 6, pp. 582–612, Nov. 2013, doi: 10.1002/WNAN.1238.

[19] A. Aliprandi, M. Mauro, and L. De Cola, “Controlling and imaging biomimetic self-assembly,” *Nature Chemistry 2015 8:1*, vol. 8, no. 1, pp. 10–15, Nov. 2015, doi: 10.1038/nchem.2383.

[20] W. H. Lee and Y. D. Park, “Tuning Electrical Properties of 2D Materials by Self-Assembled Monolayers,” *Adv Mater Interfaces*, vol. 5, no. 1, p. 1700316, Jan. 2018, doi: 10.1002/ADMI.201700316.

[21] P. Kumar, “Directed self-assembly: Expectations and achievements,” *Nanoscale Res Lett*, vol. 5, no. 9, pp. 1367–1376, Jul. 2010, doi: 10.1007/S11671-010-9696-9/FIGURES/6.

[22] M. Grzelczak, J. Vermant, E. M. Furst, and L. M. Liz-Marzán, "Directed self-assembly of nanoparticles," *ACS Nano*, vol. 4, no. 7, pp. 3591–3605, Jul. 2010, doi: 10.1021/NN100869J.

[23] R. Meyer, C. Lemire, S. K. Shaikhutdinov, and H. J. Freund, "Surface chemistry of catalysis by gold," *Gold Bull*, vol. 37, no. 1–2, pp. 72–124, 2004, doi: 10.1007/BF03215519/METRICS.

[24] J. Gong and C. B. Mullins, "Surface science investigations of oxidative chemistry on gold," *Acc Chem Res*, vol. 42, no. 8, pp. 1063–1073, Aug. 2009, doi: 10.1021/AR8002706/ASSET/IMAGES/LARGE/AR-2008-002706_0012.JPEG.

[25] N. Vogel, J. Zieleniecki, and I. Köper, "As flat as it gets: ultrasmooth surfaces from template-stripping procedures," *Nanoscale*, vol. 4, no. 13, pp. 3820–3832, Jun. 2012, doi: 10.1039/C2NR30434A.

[26] U. Maver, O. Planinšek, J. Jamnik, A. I. Hassanien, and M. Gaberšček, "Preparation of Atomically Flat Gold Substrates for AFM Measurements," *Acta Chim Slov*, vol. 59, no. 1, pp. 212–219, 2012, [Online]. Available: https://www.ncbi.nlm.nih.gov/pubmed/24061195

[27] S. Lee *et al.*, "Scanning tunneling microscopy of template-stripped au surfaces and highly ordered self-assembled monolayers," *Langmuir*, vol. 24, no. 12, pp. 5984–5987, Jun. 2008, doi: 10.1021/LA800265Q/SUPPL_FILE/LA800265Q-FILE002.PDF.

[28] J. K. Ahn, S. J. Oh, H. Park, Y. Song, S. J. Kwon, and H. B. Shin, "Vapor-phase deposition-based self-assembled monolayer for an electrochemical sensing platform," *AIP Adv*, vol. 10, no. 4, Apr. 2020, doi: 10.1063/1.5144845/1037390.

[29] K. A. Peterlinz and R. Georgiadis, “In situ kinetics of self-Assembly by surface plasmon resonance spectroscopy,” *Langmuir*, vol. 12, no. 20, pp. 4731–4740, Oct. 1996, doi: 10.1021/LA9508452.

[30] N. Lilichenko, R. Ossig, U. Glebe, U. Siemeling, F. Hubenthal, and F. Träger, “SHG studies of self-assembled monolayers of subphthalocyanines on gold,” *https://doi.org/10.1117/12.2001277*, vol. 8609, p. 860903, Mar. 2013, doi: 10.1117/12.2001277.

[31] T. Ning, L. Zhao, Y. Huo, Y. Cai, and Y. Ren, “Giant enhancement of second harmonic generation from monolayer 2D materials placed on photonic moiré superlattice,” *Nanophotonics*, vol. 12, no. 21, pp. 4009–4016, Oct. 2023, doi: 10.1515/NANOPH-2023-0124/MACHINEREADABLECITATION/RIS.

[32] O. Dannenberger, M. Buck, and M. Grunze, “Self-assembly of n-alkanethiols: A kinetic study by second harmonic generation,” *Journal of Physical Chemistry B*, vol. 103, no. 12, pp. 2202–2213, Mar. 1999, doi: 10.1021/JP983433L.

[33] C. Vericat, M. E. Vela, and R. C. Salvarezza, “Self-assembled monolayers of alkanethiols on Au(111): surface structures, defects and dynamics,” *Physical Chemistry Chemical Physics*, vol. 7, no. 18, pp. 3258–3268, Aug. 2005, doi: 10.1039/B505903H.

[34] A. L. Deering, S. M. Van Lue, and S. A. Kandel, “Ambient-pressure vapor deposition of octanethiol self-assembled monolayers,” *Langmuir*, vol. 21, no. 23, pp. 10260–10263, Nov. 2005, doi: 10.1021/LA050814Z/ASSET/IMAGES/LARGE/LA050814ZF00005.JPEG.

[35] J. Dong, A. Wang, K. Y. S. Ng, and G. Mao, “Self-assembly of octadecyltrichlorosilane monolayers on silicon-based substrates by

chemical vapor deposition," *Thin Solid Films*, vol. 515, no. 4, pp. 2116–2122, Dec. 2006, doi: 10.1016/J.TSF.2006.07.041.

[36] A. Ulman, "Formation and structure of self-assembled monolayers," *Chem Rev*, vol. 96, no. 4, pp. 1533–1554, 1996, doi: 10.1021/CR9502357.

[37] M. Ehteshamzade, T. Shahrabi, and M. G. Hosseini, "Inhibition of copper corrosion by self-assembled films of new Schiff bases and their modification with alkanethiols in aqueous medium," *Appl Surf Sci*, vol. 252, no. 8, pp. 2949–2959, Feb. 2006, doi: 10.1016/J.APSUSC.2005.05.003.

[38] M.-C. Daniel and D. Astruc, "Gold Nanoparticles: Assembly, Supramolecular Chemistry, Quantum-Size-Related Properties, and Applications toward Biology, Catalysis, and Nanotechnology," 2004, doi: 10.1021/CR030698.

[39] Q. Jin, J. A. Rodriguez, C. Z. Li, Y. Darici, and N. J. Tao, "Self-assembly of aromatic thiols on Au(111)," *Surf Sci*, vol. 425, no. 1, pp. 101–111, Apr. 1999, doi: 10.1016/S0039-6028(99)00195-8.

[40] N. Güvener, M. Oguzhan Caglayan, and Z. Altintas, "Surface plasmon resonance sensors," *Fundamentals of Sensor Technology: Principles and Novel Designs*, pp. 163–196, Jan. 2023, doi: 10.1016/B978-0-323-88431-0.00001-6.

[41] L. H. Dubois, B. R. Zegarski, and R. G. Nuzzo, "Molecular ordering of organosulfur compounds on Au(111) and Au(100): Adsorption from solution and in ultrahigh vacuum," *J Chem Phys*, vol. 98, no. 1, pp. 678–688, Jan. 1993, doi: 10.1063/1.464613.

[42] G. E. Poirier, "Characterization of organosulfur molecular monolayers on Au(111) using scanning tunneling microscopy," *Chem Rev*, vol. 97, no. 4, pp. 1117–1127, 1997, doi:

10.1021/CR960074M/ASSET/IMAGES/LARGE/CR960074MF00009.JPEG.

[43] G. E. Poirier, “Characterization of organosulfur molecular monolayers on Au(111) using scanning tunneling microscopy,” *Chem Rev*, vol. 97, no. 4, pp. 1117–1127, 1997, doi: 10.1021/CR960074M.

[44] T. Baše *et al.*, “Carboranethiol-modified gold surfaces. A study and comparison of modified cluster and flat surfaces,” *Langmuir*, vol. 21, no. 17, pp. 7776–7785, Aug. 2005, doi: 10.1021/LA051122D/SUPPL_FILE/LA051122DSI20050707_115429.PDF.

[45] J. J. Schwartz *et al.*, “Surface dipole control of liquid crystal alignment,” *J Am Chem Soc*, vol. 138, no. 18, pp. 5957–5967, May 2016, doi: 10.1021/JACS.6B02026/ASSET/IMAGES/JA-2016-020264_M015.GIF.

[46] J. Kim *et al.*, “Interface control in organic electronics using mixed monolayers of carboranethiol isomers,” *Nano Lett*, vol. 14, no. 5, pp. 2946–2951, May 2014, doi: 10.1021/NL501081Q/SUPPL_FILE/NL501081Q_SI_001.PDF.

[47] J. N. Hohman *et al.*, “Self-Assembly of carboranethiol isomers on Au{111}: Intermolecular interactions determined by molecular dipole orientations,” *ACS Nano*, vol. 3, no. 3, pp. 527–536, Mar. 2009, doi: 10.1021/NN800673D.

[48] J. C. Thomas *et al.*, “Self-Assembled p-Carborane Analogue of p-Mercaptobenzoic Acid on Au{111},” *Chemistry of Materials*, vol. 27, no. 15, pp. 5425–5435, Aug. 2015, doi: 10.1021/ACS.CHEMMATER.5B02263/SUPPL_FILE/CM5B02263_SI_004.XYZ.

[49] K. E. White *et al.*, “Competing Intermolecular and Molecule-Surface Interactions: Dipole-Dipole-Driven Patterns in Mixed Carborane Self-Assembled Monolayers,” *Chemistry of Materials*, vol. 36, no. 4, pp. 2085–2095, Feb. 2024, doi: 10.1021/ACS.CHEMMATER.3C03210/ASSET/IMAGES/LARGE/CM3C03210_0007.JPEG.

[50] M. Yortanll, M. F. Danlşman, and E. Mete, “Functional Group Effects on the Electrochemical Properties of Carboranethiol Monolayers on Au(111) As Studied by Density Functional Theory: Implications for Organic Electronics,” *ACS Appl Nano Mater*, vol. 5, no. 8, pp. 11185–11193, Aug. 2022, doi: 10.1021/ACSANM.2C02339.

[51] A. S. Duwez, “Exploiting electron spectroscopies to probe the structure and organization of self-assembled monolayers: a review,” *J Electron Spectros Relat Phenomena*, vol. 134, no. 2–3, pp. 97–138, Feb. 2004, doi: 10.1016/J.ELSPEC.2003.10.005.

[52] R. K. Smith, P. A. Lewis, and P. S. Weiss, “Patterning self-assembled monolayers,” *Prog Surf Sci*, vol. 75, no. 1–2, pp. 1–68, Jun. 2004, doi: 10.1016/J.PROGSURF.2003.12.001.

[53] D. Y. Kwok and A. W. Neumann, “Contact angle measurement and contact angle interpretation,” *Adv Colloid Interface Sci*, vol. 81, no. 3, pp. 167–249, Sep. 1999, doi: 10.1016/S0001-8686(98)00087-6.

[54] T. Baše, J. Macháček, Z. Hájková, J. Langecker, J. D. Kennedy, and M. J. Carr, “Thermal isomerizations of monothiolated carboranes (HS)C2B10H11 and the solid-state investigation of 9-(HS)-1,2-C2B10H11 and 9-(HS)-1,7-C2B10H11,” *J Organomet Chem*, vol. 798, pp. 132–140, Dec. 2015, doi: 10.1016/J.JORGANCHEM.2015.06.020.

[55] P. Wagner, M. Hegner, P. Kernen, F. Zaugg, and G. Semenza, "Covalent immobilization of native biomolecules onto Au(111) via N-hydroxysuccinimide ester functionalized self-assembled monolayers for scanning probe microscopy," *Biophys J*, vol. 70, no. 5, pp. 2052–2066, May 1996, doi: 10.1016/S0006-3495(96)79810-7.

[56] M. Hegner, P. Wagner, and G. Semenza, "Ultralarge atomically flat template-stripped Au surfaces for scanning probe microscopy," *Surf Sci*, vol. 291, no. 1–2, pp. 39–46, Jul. 1993, doi: 10.1016/0039-6028(93)91474-4.

[57] C. D. Bain, E. B. Troughton, Y. T. Tao, J. Evall, G. M. Whitesides, and R. G. Nuzzo, "Formation of Monolayer Films by the Spontaneous Assembly of Organic Thiols from Solution onto Gold," *J Am Chem Soc*, vol. 111, no. 1, pp. 321–335, 1989, doi: 10.1021/JA00183A049/SUPPL_FILE/JA00183A049_SI_001.PDF.

[58] A. Yavuz, "Investigation of perfluoropentacene thin films on substrates with different chemical structures," Middle East Technical University, 2020.

[59] R. J. Martín-Palma and A. Lakhtakia, "Vapor-Deposition Techniques," *Engineered Biomimicry*, pp. 383–398, Jan. 2013, doi: 10.1016/B978-0-12-415995-2.00015-5.

[60] S. J. Grutzik, R. S. Gates, Y. B. Gerbig, D. T. Smith, R. F. Cook, and A. T. Zehnder, "Accurate spring constant calibration for very stiff atomic force microscopy cantilevers," *Review of Scientific Instruments*, vol. 84, no. 11, Nov. 2013, doi: 10.1063/1.4832978/358706.

[61] T. A. Efimov, E. A. Rassolov, B. G. Andryukov, T. S. Zaporozhets, and R. V. Romashko, "Calculation of Resonant Frequencies of

Silicon AFM Cantilevers," *J Phys Conf Ser*, vol. 1439, no. 1, p. 012006, Jan. 2020, doi: 10.1088/1742-6596/1439/1/012006.

[62] A. Dzedzickis, J. Rožėnė, V. Bučinskas, D. Viržonis, and I. Morkvėnaitė-Vilkončienė, "Characteristics and Functionality of Cantilevers and Scanners in Atomic Force Microscopy," *Materials 2023, Vol. 16, Page 6379*, vol. 16, no. 19, p. 6379, Sep. 2023, doi: 10.3390/MA16196379.

[63] G. Stan and S. W. King, "Atomic force microscopy for nanoscale mechanical property characterization," *Journal of Vacuum Science & Technology B, Nanotechnology and Microelectronics: Materials, Processing, Measurement, and Phenomena*, vol. 38, no. 6, Nov. 2020, doi: 10.1116/6.0000544/588943.

[64] H. Y. Erbil, "The debate on the dependence of apparent contact angles on drop contact area or three-phase contact line: A review," *Surf Sci Rep*, vol. 69, no. 4, pp. 325–365, Dec. 2014, doi: 10.1016/J.SURFREP.2014.09.001.

[65] H. Yildirim Erbil, N. Gao, and V. Starov, "Dependency of Contact Angles on Three-Phase Contact Line: A Review," *Colloids and Interfaces 2021, Vol. 5, Page 8*, vol. 5, no. 1, p. 8, Feb. 2021, doi: 10.3390/COLLOIDS5010008.

[66] A. Rudawska and E. Jacniacka, "Evaluating uncertainty of surface free energy measurement by the van Oss-Chaudhury-Good method," *Int J Adhes Adhes*, vol. 82, pp. 139–145, Apr. 2018, doi: 10.1016/J.IJADHADH.2018.01.006.

[67] D. Y. Kwok and A. W. Neumann, "Contact angle interpretation in terms of solid surface tension," *Colloids Surf A Physicochem Eng Asp*, vol. 161, no. 1, pp. 31–48, Jan. 2000, doi: 10.1016/S0927-7757(99)00323-4.

[68] H. Tavana and A. W. Neumann, “Recent progress in the determination of solid surface tensions from contact angles,” *Adv Colloid Interface Sci*, vol. 132, no. 1, pp. 1–32, Mar. 2007, doi: 10.1016/J.CIS.2006.11.024.

[69] E. Langereis, S. B. S. Heil, H. C. M. Knoops, W. Keuning, M. C. M. Van De Sanden, and W. M. M. Kessels, “In situ spectroscopic ellipsometry as a versatile tool for studying atomic layer deposition,” *J Phys D Appl Phys*, vol. 42, no. 7, p. 073001, Mar. 2009, doi: 10.1088/0022-3727/42/7/073001.

[70] E. Garcia-Caurel, A. De Martino, J. P. Gaston, and L. Yan, “Application of spectroscopic ellipsometry and mueller ellipsometry to optical characterization,” *Appl Spectrosc*, vol. 67, no. 1, pp. 1–21, Jan. 2013, doi: 10.1366/12-06883/ASSET/IMAGES/LARGE/10.1366_12-06883-FIG16.JPEG.

[71] R. L. Olmon *et al.*, “Optical dielectric function of gold,” *Phys Rev B Condens Matter Mater Phys*, vol. 86, no. 23, Dec. 2012, doi: 10.1103/PHYSREVB.86.235147/OLMON_PRB2012_TS.PDF.

[72] D. N. G. Krishna and J. Philip, “Review on surface-characterization applications of X-ray photoelectron spectroscopy (XPS): Recent developments and challenges,” *Applied Surface Science Advances*, vol. 12, p. 100332, Dec. 2022, doi: 10.1016/J.APSADV.2022.100332.

[73] G. Greczynski and L. Hultman, “X-ray photoelectron spectroscopy: Towards reliable binding energy referencing,” *Prog Mater Sci*, vol. 107, p. 100591, Jan. 2020, doi: 10.1016/J.PMATSCI.2019.100591.

[74] D. A. L. Leelamanie and J. Karube, “Drop size dependence of soil-water contact angle in relation to the droplet geometry and line tension,” *Soil Sci Plant Nutr*, vol. 58, no. 6, pp. 675–683, Dec. 2012, doi: 10.1080/00380768.2012.745798.

[75] A. Amirfazli, D. Y. Kwok, J. Gaydos, and A. W. Neumann, “Line Tension Measurements through Drop Size Dependence of Contact Angle,” *J Colloid Interface Sci*, vol. 205, no. 1, pp. 1–11, Sep. 1998, doi: 10.1006/JCIS.1998.5562.

[76] H. Tavana and A. W. Neumann, “On the question of rate-dependence of contact angles,” *Colloids Surf A Physicochem Eng Asp*, vol. 282–283, pp. 256–262, Jul. 2006, doi: 10.1016/J.COLSURFA.2006.01.001.

[77] D. G. Castner, K. Hinds, and D. W. Grainger, “X-ray photoelectron spectroscopy sulfur 2p study of organic thiol and bisulfide binding interactions with gold surfaces,” *Langmuir*, vol. 12, no. 21, pp. 5083–5086, Oct. 1996, doi: 10.1021/LA960465W.

[78] D. P. Goronzy *et al.*, “Influence of Terminal Carboxyl Groups on the Structure and Reactivity of Functionalized m-Carboranethiolate Self-Assembled Monolayers,” *Chemistry of Materials*, vol. 32, no. 15, pp. 6800–6809, Aug. 2020, doi: 10.1021/ACS.CHEMMATER.0C02722/SUPPL_FILE/CM0C02722_SI_003.CIF.

[79] F. L. Pasquale, Y. Li, J. Du, and J. A. Kelber, “Novel alloy polymers formed from ortho-carborane and benzene or pyridine,” *Journal of Physics: Condensed Matter*, vol. 25, no. 10, p. 105801, Feb. 2013, doi: 10.1088/0953-8984/25/10/105801.

[80] H. U. Yang, J. D’Archangel, M. L. Sundheimer, E. Tucker, G. D. Boreman, and M. B. Raschke, “Optical dielectric function of silver,” *Phys Rev B Condens Matter Mater Phys*, vol. 91, no. 23, Jun. 2015, doi: 10.1103/PHYSREVB.91.235137/SUPPORTING_INFORMATION.PDF.